Multi-static synthetic aperture radar and inverse scattering

Gustafsson, Mats

2004

CODEN:LUTEDX/(TEAT-7123)/1-28/(2003)

Multi-static synthetic aperture radar and inverse scattering

Mats Gustafsson

Department of Electroscience
Electromagnetic Theory
Lund Institute of Technology
Sweden

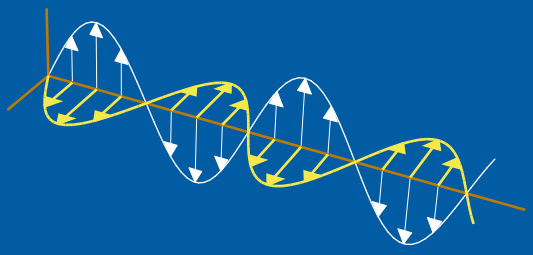

Mats Gustafsson

Department of Electroscience
Electromagnetic Theory
Lund Institute of Technology
P.O. Box 118
SE-221 00 Lund
Sweden

Editor: Gerhard Kristensson

Abstract

In this paper synthetic aperture radar is analyzed from an inverse scattering perspective. It is shown that the classical point scattering model can be generalized to a dipole scattering model. The dipole scattering model reduces to the point scattering model for small aperture angles. For large aperture angles or multiple illumination apertures the dipole model gives an anisotropic reflectivity such that orthogonal scattering processes are separated. Moreover, it is shown that both the point and dipole scattering models can be interpreted as an initial step of a least-squares inverse scattering algorithm.

1 Introduction

The resolution in radar imaging systems is determined by the bandwidth, center frequency, and imaging aperture. In Synthetic Aperture Radar (SAR) a small antenna is moved along a convenient path (here the flight track) to form a long antenna and hence a large imaging aperture [1, 3, 7, 10, 18]. One distinguish between strip, scan, and spot mode SAR systems. In this paper, the focus is on the spot mode that offers a high resolution but narrow coverage. The CARABAS-II and LORA systems operate in the MHz regime, see Table 1. In this frequency range, the radar signals penetrate tree coverage and can hence be used to image concealed objects. The radar echoes due to ground scattering are also reduced. However, the typical resolution of these systems are not as good as of the GHz systems [16].

In this paper, multi-static SAR systems are analyzed. Here, it is important to find the correct balance between the existence of a solution and the uniqueness of the same solution, *i.e.*, to find a simple and accurate scattering model that can be used to model the interaction between the considered objects and the used electromagnetic fields. The traditional SAR model is based on the point scatterer model [1, 3, 7, 10, 18]. This, very successful, model is good for high frequency systems with a moderate aperture angle. To overcome some of its artifacts, point scatter fixes can be used [3, 8]. These parametric models are typically based on high frequency approximations, *e.g.*, GTD. For low-frequency systems with a large aperture angle or multi-static operation it is also observed that the point scatter model is not satisfying. In this paper it is shown that a simple anisotropic scattering model based on a dipole scattering model can be used for these systems.

The paper begins with a discussion on SAR imaging and inverse scattering in Section 2. The point scattering model is considered in Section 3 and the dipole scattering model is considered in Section 4. In Section 6, it is shown that both the point scattering model and the dipole scattering model can be interpreted as an initial step of a least-squares inverse scattering algorithm. In Section 7, the results are discussed.

System	frequency	wavelength
CARABAS-II (VHF-band)	$20-90\,\mathrm{MHz}$	$3.3-15\,\mathrm{m}$
LORA (UHF-band)	$195-755\,\mathrm{MHz}$	$0.4-1.5\,\mathrm{m}$
L-band	$1-2\,\mathrm{GHz}$	$15-30\,\mathrm{cm}$
S-band	$2-4\,\mathrm{GHz}$	$7.5-15\,\mathrm{cm}$
C-band	$4-8\,\mathrm{GHz}$	$3.8-7.5\,\mathrm{cm}$
X-band	$8-12\,\mathrm{GHz}$	$2.5-3.8\,\mathrm{cm}$

Table 1: Example of SAR systems. The CARABAS-II system has a relatively low frequency compared with the common L,S,C, and X band systems.

2 Synthetic aperture radar and inverse scattering

2.1 SAR data

In Figure 1, the typical SAR setup is illustrated. The object is illuminated with an electromagnetic (EM) wave transmitted from an airplane. It is also common to use satellites and space shuttles. The scattered EM wave field is received by a receiver. The mono-static or back-scattered case where the transmitter and receiver are located at the same position is the most well known case [7, 10, 16, 18, 19]. The bi-static case, where the transmitter and receiver are located in different points has also received a great deal of attention [17]. In a multi-static setup several transmitters and receivers surrounding the object are considered. Typically, the receivers and transmitters are located on a path (the flight track) far from the illuminated object. In this paper, it is assumed that the transmitters and receivers are located in the far-field of the object. The transmitter and receiver positions are denoted $\boldsymbol{r}_{\mathrm{t}}$ and $\boldsymbol{r}_{\mathrm{r}}$, respectively. The transmitter and receiver positions are given by the flight track, *e.g.*, $\boldsymbol{r}_{\mathrm{t}} = \boldsymbol{r}_{\mathrm{t}}(\tau)$, where τ is a parameterization of the path that generates the flight track. Observe that although the mono-static case $\boldsymbol{r}_{\mathrm{t}}(\tau) = \boldsymbol{r}_{\mathrm{r}}(\tau)$ and the bi-static case $\boldsymbol{r}_{\mathrm{t}}(\tau) \neq \boldsymbol{r}_{\mathrm{r}}(\tau)$ are the most commonly considered cases, it is easy to generalize the setup to a multi-static case with several transmitters and receivers.

The transmitted field $\boldsymbol{E}$ from the direction $-\hat{\boldsymbol{k}}$ is approximated with a plane wave

$$\boldsymbol{E}(\boldsymbol{x}, t) = \boldsymbol{E}_0 p(t - \hat{\boldsymbol{k}} \cdot \boldsymbol{x}/c_0), \tag{2.1}$$

where $p(t)$ is the pulse shape. The corresponding transmitted field in the wavenumber domain is given by

$$\boldsymbol{E}(\boldsymbol{x}, \boldsymbol{k}) = \boldsymbol{E}_0(\boldsymbol{k})\mathrm{e}^{-\mathrm{i}\boldsymbol{k}\cdot\boldsymbol{x}}, \tag{2.2}$$

where $\boldsymbol{k} = k\hat{\boldsymbol{k}}$ and k is the wavenumber $k = 2\pi f/c_0 = 2\pi/\lambda$. The related scattered field is of the form

$$\boldsymbol{E}(\boldsymbol{r}, \boldsymbol{k}) = \frac{\mathrm{e}^{-\mathrm{i}kr}}{kr}\boldsymbol{F}(\hat{\boldsymbol{r}}, \boldsymbol{k}) \tag{2.3}$$

where $\boldsymbol{F}$ is the far-field pattern. The map from the incident plane wave to the

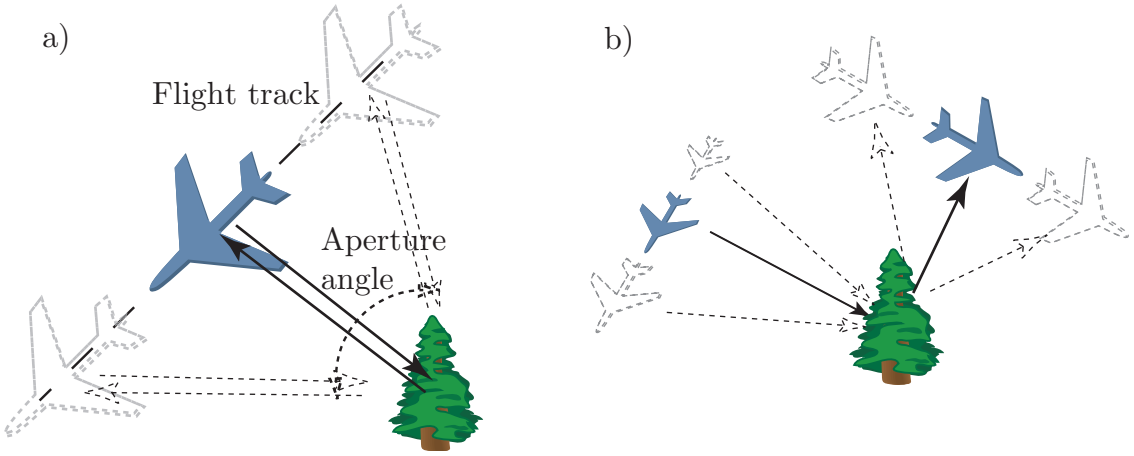

Figure 1: Illustration of the SAR setup. a) in the mono-static (backscattering) case, a single airplane is used both to transmit and receive the radar signal. b) in the bi-static case separate airplanes are used as transmitters and receivers. An arbitrary number of airplanes can be used in multi-static cases.

scattered field is called the scattering dyad (or scattering matrix) [12], *i.e.*,

$$\boldsymbol{F}(\hat{\boldsymbol{r}}, \boldsymbol{k}) = \mathbf{S}(\hat{\boldsymbol{r}}, \boldsymbol{k})\boldsymbol{E}_0(\boldsymbol{k}). \tag{2.4}$$

Mono-static and bi-static SAR data consist of the far-field pattern (or scattering matrix) given for a range of wavenumbers $k_1 \leq k \leq k_2$ together with the plane wave direction $\hat{\boldsymbol{k}}(\tau)$ and the corresponding observation direction $\hat{\boldsymbol{r}}(\tau)$ along a path $0 \leq \tau \leq T$. Multi-static data can be given for many different configurations. In this paper it is sufficient to consider the multi-static SAR data given by the far-field patterns for a range of wavenumbers $k_1 \leq k \leq k_2$ together with N plane wave directions $\hat{\boldsymbol{k}}_n(\tau_n), n = 1, ..., N$ and M corresponding observation directions $\hat{\boldsymbol{r}}_{mn}(\tau_n), m = 1, ..., M_n$ along the N paths $0 \leq \tau_n \leq T_n$. Spherical coordinates $\{\theta, \phi\}$ are used to parameterize the illumination angle and observation angle, *i.e.*,

$$\hat{\boldsymbol{k}} = (\cos\phi_{\mathrm{i}} \sin\theta_{\mathrm{i}}, \sin\phi_{\mathrm{i}} \sin\theta_{\mathrm{i}}, \cos\theta_{\mathrm{i}}) \quad \text{and} \quad \hat{\boldsymbol{r}} = (\cos\phi_{\mathrm{o}} \sin\theta_{\mathrm{o}}, \sin\phi_{\mathrm{o}} \sin\theta_{\mathrm{o}}, \cos\theta_{\mathrm{o}}) \tag{2.5}$$

where θ is the elevation angle and ϕ is the azimuthal angle. It is common to consider a fixed elevation angle and to let the flight track be parametrized by the azimuthal angle $\phi_1 \leq \phi \leq \phi_2$. For a low flight track, $\theta \approx 90°$, the aperture angle is approximately $\phi_2 - \phi_1$.

2.2 Inverse scattering theory related to SAR

SAR is often analyzed from an imaging perspective, where a scalar reflectivity is used to model the scattering object [2, 18], see Section 3. This leads to linear inverse problems analog to tomography [18]. Although, this approach is very successful for typical mono-static narrow angle SAR systems it is necessary to improve theses

models for general multi-static SAR systems. SAR can also be analyzed from an inverse scattering perspective where material parameters such as permittivity and conductivity of penetrable objects and the shape of impenetrable objects are used to model the scattering object. In this case Colton-Kress gives several uniqueness theorems [6]. For example the shape of an object is uniquely determined by the far-field data if

- the far-field pattern is given for all incident directions and all polarizations at one single frequency, *i.e.*, $\boldsymbol{F}(\hat{\boldsymbol{r}}, k\hat{\boldsymbol{k}})$ is given for all $\hat{\boldsymbol{r}}$, all $\hat{\boldsymbol{k}}$, and a fixed k, see Theorem 7.1 in [6].

- the far-field pattern is given for some directions and the object is sufficiently small.

- the far-field pattern is given in one direction and one polarization for a range of wavenumbers, *i.e.*, $\boldsymbol{F}(\hat{\boldsymbol{r}}, k\hat{\boldsymbol{k}})$ is given for all $\hat{\boldsymbol{r}}$, one $\hat{\boldsymbol{k}}$, and an interval $k_1 < k < k_2$, see Theorem 7.2 in [6].

There are also several theorems for the uniqueness of medium parameters. For example the index of refraction (permittivity) is uniquely determined by the far-field data under similar circumstances. The third case is the most interesting case for SAR. However, it is important to notice that although the object shape is uniquely determined by the far-field data, the shape does not depend continuously on the data. Small errors in the data (noise) can give large errors in the shape. Also observe that the theorems in [6] require a lot of data, *i.e.*, the complete far-field pattern. Unfortunately, the theorems do not give any information about the case with limited data such as bi-static and multi-static data.

The are a few non-linear inversion algorithms. One is the linear sampling method by Colton and Kirsch. The linear sampling method determines the shape of an object from multi-static data at a fixed frequency [5]. A comparison between the linear sampling method and the linearized tomographic inverse scattering algorithm is given in [4], see also [15] for comparisons between linear and non-linear inversion algorithms.

Non-linear optimization have received a lot of attention the last couple of years. Theses algorithms often iterative and require numerical solutions of the direct scattering problem for each iteration. Hence, these algorithms are generally slow and require fast forward solvers. However, there are algorithms that can be more efficient [11]. Their advantage is that the formulation is general and can hence be applied to many problems. A typical formulation is $\min_{\text{parameters}} \|u_{\text{measured}} - u_{\text{calc}}\| + \|u_{\text{calc}}\|_{\text{reg}}$ where the second term is the regularization. After proper choices of the norms and tuning of all variables it is just to choice a standard optimization algorithm. It is common to differentiate between global optimization algorithms and local optimization algorithms. The local optimization algorithms uses some kind of gradient estimate to find the locally best direction to update the parameters. In this paper a time domain least-squares algorithm is used for the SAR problem with multi-static data, see Section 6.

3 Point scattering model

One of the simplest ways to derive a SAR imaging algorithm is to use the point scattering model or scalar reflectivity model. In this model the vector nature of the EM field is neglected and scalar fields are used. Let E_0 represent the incident field, *i.e.*, $\boldsymbol{E}_0 = E_0\hat{\boldsymbol{\phi}}$ and $\boldsymbol{E}_0 = E_0\hat{\boldsymbol{\theta}}$ for a horizontally and vertically polarized antenna, respectively. The received field is assumed to be co-polarized, *i.e.*, the scalar far-field pattern F is defined as $\boldsymbol{F} = F\hat{\boldsymbol{\phi}}$ and $\boldsymbol{F} = F\hat{\boldsymbol{\theta}}$ in the horizontal and vertical cases, respectively. The point scattering model gives the far-field pattern F

$$F(\hat{\boldsymbol{r}}, \boldsymbol{k}) = \int_\Omega E_0(\boldsymbol{k})\mathrm{e}^{-\mathrm{i}\boldsymbol{k}\cdot\boldsymbol{x}}k^3\gamma(\boldsymbol{x})\mathrm{e}^{\mathrm{i}k\hat{\boldsymbol{r}}\cdot\boldsymbol{x}}\,\mathrm{dV}_{\boldsymbol{x}} = \int_\Omega k^3E_0(\boldsymbol{k})\mathrm{e}^{-\mathrm{i}(\boldsymbol{k}_\mathrm{i}-k\hat{\boldsymbol{r}})\cdot\boldsymbol{x}}\gamma(\boldsymbol{x})\,\mathrm{dV}_{\boldsymbol{x}}, \quad (3.1)$$

where $\gamma(\boldsymbol{x})$ is the scalar reflectivity. Here, it is seen that there is a Fourier type relation between the far-field pattern and the reflectivity. The k^3 factor in this model is motivated by the scattering properties of a small sphere, *i.e.*, the scattering amplitude of a sphere with radius a is proportional to a^3k^3 if $ka \ll 1$. However, different weight factors can be used. Although the discussion here is limited to scalar reflectivity it can be extended to polarimetric SAR by inclusion of the cross-polarized far-field pattern [13].

In the mono-static case $k\hat{\boldsymbol{r}} = -\boldsymbol{k}$, the result simplifies to

$$F(\boldsymbol{k}) = \int_\Omega k^3E_0(\boldsymbol{k})\gamma(\boldsymbol{x})\mathrm{e}^{-\mathrm{i}2\boldsymbol{k}\cdot\boldsymbol{x}}\,\mathrm{dV}_{\boldsymbol{x}}\,. \quad (3.2)$$

Formal inversion of the Fourier integral (3.2) gives

$$\gamma(\boldsymbol{x}) = \frac{1}{8\pi^3}\int_{\boldsymbol{k}\in\mathbb{R}^3}\frac{1}{k^3}\frac{E_0^*(\boldsymbol{k})F(\boldsymbol{k})}{|E_0(\boldsymbol{k})|^2}\mathrm{e}^{\mathrm{i}2\boldsymbol{k}\cdot\boldsymbol{x}}\,\mathrm{dV}_{\boldsymbol{k}}, \quad (3.3)$$

i.e., the scalar reflectivity is given by the Fourier transform of the scattering dyad, *cf.* (2.4). It is also interesting to compare with the physical optics approximation [12]. The physical optics approximation is valid for convex perfectly conducting objects that are smooth relative the wave length. The support of the object is given by

$$\gamma_{\mathrm{po}}(\boldsymbol{x}) = \frac{1}{8\pi^2}\int\frac{1}{k^3}\left(\frac{E_0^*(\boldsymbol{k})F(\boldsymbol{k})}{|E_0(\boldsymbol{k})|^2} + \frac{E_0(-\boldsymbol{k})F^*(-\boldsymbol{k})}{|E_0(-\boldsymbol{k})|^2}\right)\mathrm{e}^{\mathrm{i}2\boldsymbol{k}\cdot\boldsymbol{x}}\,\mathrm{dV}_{\boldsymbol{k}}\,. \quad (3.4)$$

The occurrence of the two terms in the integral is related to the physical optics approximation, *i.e.*, only illuminated part of the object is used.

The Fourier transform requires knowledge of the scattering dyad for all directions and all frequencies. In general, SAR data is never given for all frequencies and all directions, in these cases the reflectivity is typically given by (3.3) over the available data. In typical mono-static and bi-static flight paths (2.5), the reflectivity is determined for fixed heights z, here $z = 0$. The scalar reflectivity (3.1) can hence be inverted by spectral data in a plane, *e.g.*, a mono-static flight path around the object for all frequencies. The support in the wavenumber domain is given by

$$k(\hat{\boldsymbol{k}}(\tau) - \hat{\boldsymbol{r}}(\tau)), \quad \text{for} \quad k_1 \le k \le k \text{ and } 0 \le \tau \le \Upsilon. \quad (3.5)$$

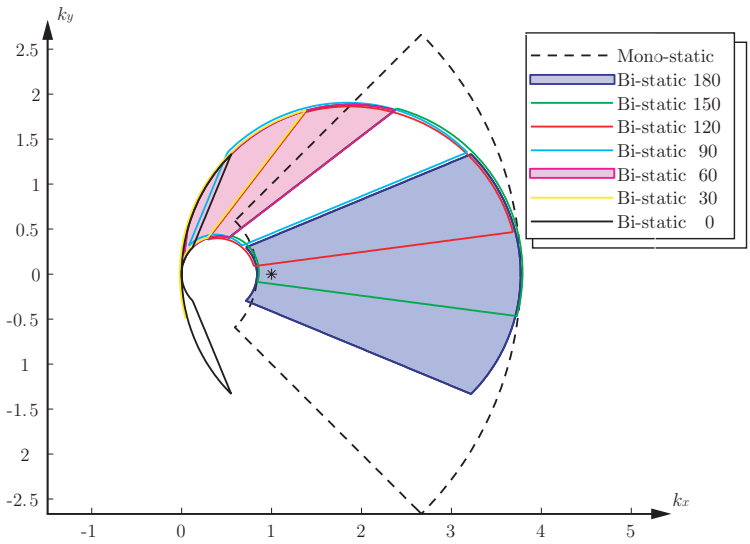

Figure 2: Spectral coverage for mono-static and bi-static setups with a 90° aperture angle. The mono-static case has the largest spectral coverage and the spectral coverage of the bi-static cases increases as the scattering angle increases.

The wavenumber domain for mono-static and bi-static setups with a 90° aperture angle and CARABAS-II frequencies is depicted in Figure 2. The mono-static case has the largest spectral coverage. The spectral coverage of the bi-static case has its maximum in back-scattering and direction decreases as the scattering angle decreases. Also observe that the wavenumber domain mainly changes in the direction of the illumination.

3.1 Interference and anisotropy

The scalar point-like scattering model is based on the assumption that the object consists of a collection of single scattering objects. Moreover, the scattering is often assumed to be isotropic and non-dispersive. Unfortunately, the scattering of most SAR objects are very complex and these approximations are in general not valid. However, the point-like model is widely used and there is a massive amount of successful SAR images based on this model, so the approximation must be rather good under normal SAR circumstances.

The complex scattering properties of typical SAR objects are due to three properties. First, a typical SAR object is in a wave length scale or smaller for CARABAS-II frequencies whereas several wave lengths for X band systems. This gives typically anisotropic properties in the low frequency regime, dispersive properties in the resonance regime, and oblique scattering properties in the high frequency regime, respectively. Secondly, the dominant scattering process is often multiple scattering paths incorporating both the object and the ground. Finally, multiple scattering between separated objects can also contribute to the total scattering. In this paper, the first processes with single object scattering are analyzed. The problem with a

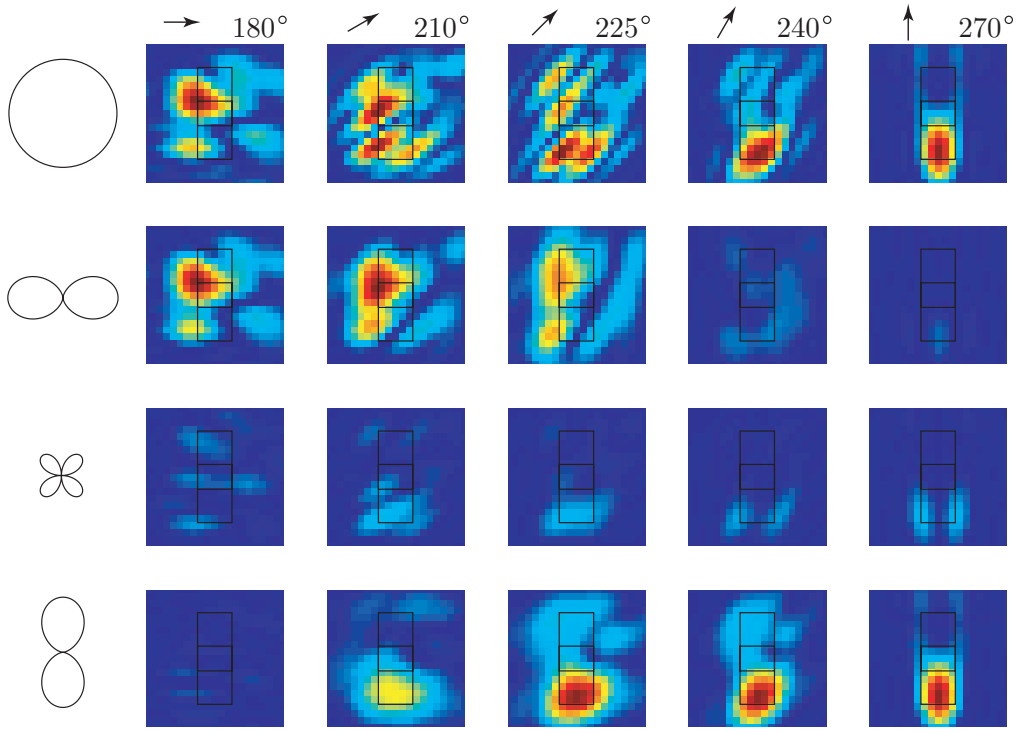

Figure 3: Comparison between the SAR images with a point source (top row) and SAR images with a directional dependence. The directional dependence is given by the weight patterns shown to the left of the images. The flight track is between 180° to 270° with an average illumination indicated by the arrows.

ground reflection can reduced by incorporation of a layered wave propagation model.

In [16], computer simulations have been performed to analyze SAR images for the CARABAS-II and LORA systems, see Table 1 and the top row of Figure 3. A Swedish military terrain vehicle with dimensions of approximately 2.5 m × 3 m × 6.5 m, modeled as a perfect electric conductor (PEC), standing on a ground with permittivity $\epsilon_r = 10$ and conductivity $\sigma = 0.01$ S/m is used as scattering object. The object is illuminated from a 90° flight track at elevation angle $\theta_o = 50°$ with normal direction between 180° and 270° as indicated by the arrows under each image in the top row in Figure 3. In the figure, it is observed that the scalar reflectivity model gives good results for the case with broad side illumination, *i.e.*, the first and last cases.

In the other cases with illumination both from the side and front of the vehicle, the images appear irregular. This irregular behavior is due to a sort of interference between the two dominant scattering processes in these images, *i.e.*, the oblique scattering from the side and front of the vehicle, see also Figure 4. These parts of the scattering process are clearly visible in the lower parts the Figure 3. In the second to fourth row of Figure 3, the SAR images weighted with directional patterns depicted to the left of the images are shown. Scattering processes related to the left-right and up-down directions are shown in the second and fourth row,

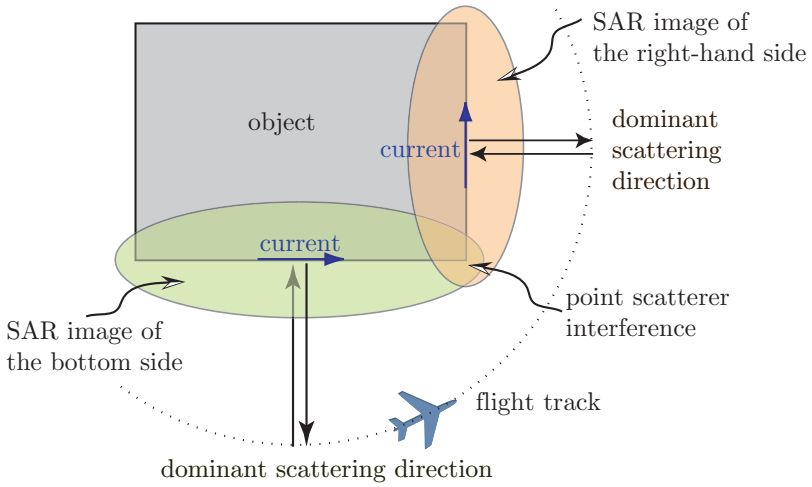

Figure 4: Illustration of the point scatter interference. The interference is due to addition of complex valued image parts originating from different scattering processes.

respectively.

Notice that the image contents of the 180° images, with an illumination from the left, is found in the second row and similarly, the 270° images, with an illumination from below is found in the fourth row. In these two cases, it is also observed that the point scattering model with an isotropic weight pattern gives good results. However, for the 210° and 225° cases, there are image contributions in more than one row. The scattering from the side of the vehicle is seen in the second row and the scattering from the front is seen in the fourth row.

3.2 Bi-static and multi-static data

Assuming the point scattering model (3.1), there is clearly a unique image for the case of mono-static data given for all wave numbers. This image also depends continuously on the data, *i.e.*, the Fourier transform is a continuous map. It is also clear that there exist such an image. So where is the problem with the point scattering model? One problem is that it is not clear how the point scattering image relates to the actual object properties, *i.e.*, the shape of PEC objects and permittivity and conductivity of penetrable objects, see Figure 3. Another problem is that it is not possible to add data consistently, *i.e.*, in general there is no solution if more data is provided, *e.g.*, bi-static or multi-static data. For these cases, a more accurate scattering model has to be used.

To illustrate the requirements of the SAR scattering model, the scattering properties of a plate, a wedge, and a non-connected wedge is considered. The mono-static radar cross section of the plate and a wedge and bi-static radar cross section of a plate is depicted in Figures 5, 6, and 7, respectively. The plate is $1\,\mathrm{m} \times 1\,\mathrm{m}$ and the wedge is composed of two plates. The plate is oriented with its normal in the x-direction and the wedge has its normal in the x-direction and y-direction. The

mono-static RCS is given for the flight path $\theta = 90°$ and $0 \leq \phi \leq 360°$. The vertical (TE) and horizontal (TM) cases are given by a $\hat{\boldsymbol{\theta}}$ (orthogonal to the flight path) and $\hat{\boldsymbol{\phi}}$ (parallel with the flight path) polarization, respectively. The RCS is calculated with the method of moments using an equidistant triangularization (with 1 dm side) and RWG basis functions [14].

As seen in the figures, the radar cross section depends strongly on the illumination angle for the horizontal case. Observe that the objects are 1 m to 2 m and hence much smaller than the wave length for the frequencies 20 MHz (15 m) and 55 MHz (5.5 m), *i.e.*, the objects are to be considered as point scatterers for these frequencies. The almost constant RCS in the vertical case can be explained by the induced currents, that are orthogonal to the flight path and hence radiates omni directionally for small objects. The vector nature of the EM field can be neglected and the point scatterer model is valid. However, the vector nature of the EM field is crucial in the horizontal case. In this case, the currents are induced parallel with the flight path and can contribute both constructively and destructively to the back scattered field. The RCS of the plate is zero for the grazing illumination , *i.e.*, $\phi = 90°$ and $\phi = 270°$. Comparing with the point-scatterer model, that predicts that the scattering is independent of the incident angle and polarization, it is noticed that the point scatterer model is only valid for the vertical case. For the horizontal case it is necessary to incorporate the vector nature of the EM fields in the model. This can be done with an anisotropic scattering model, *e.g.*, a model based on the scattering properties of a short wire, *i.e.*, a dipole.

4 Dipole scattering model

4.1 Dipole scatterer model and anisotropic reflectivity

The scattering from a short wire is in the form of a dipole pattern. The scattered field from a short dipole with direction $\hat{\boldsymbol{d}}$ is proportional to the incident electric field projected on the dipole $\boldsymbol{E} \cdot \hat{\boldsymbol{d}}$ and the far-field pattern is $\boldsymbol{F}_{\boldsymbol{d}}(\hat{\boldsymbol{r}}) \sim \hat{\boldsymbol{\theta}}$, where θ is the angle between $\boldsymbol{d}$ and $\hat{\boldsymbol{r}}$. With the dipole moment $\boldsymbol{p}$, the far-field pattern is

$$\boldsymbol{F}(\hat{\boldsymbol{r}}) = \frac{k^3}{4\pi\epsilon_0} \hat{\boldsymbol{r}} \times (\boldsymbol{p} \times \hat{\boldsymbol{r}}). \tag{4.1}$$

In general, the magnetic dipole can also contribute to the scattering, *i.e.*, the scattering from a small object is given by

$$\boldsymbol{F}(\hat{\boldsymbol{r}}) = \frac{k^3}{4\pi\epsilon_0} \left(\hat{\boldsymbol{r}} \times (\boldsymbol{p} \times \hat{\boldsymbol{r}}) + \epsilon_0 \mu_0 \boldsymbol{m} \times \hat{\boldsymbol{r}} \right). \tag{4.2}$$

With an incident plane wave $\boldsymbol{E}(\boldsymbol{x}, \tau, k) = \boldsymbol{E}_0 \mathrm{e}^{-\mathrm{i}k\hat{\boldsymbol{k}}\cdot\boldsymbol{x}}$ and assuming single scattering of electrical dipole type, the scattered field is

$$\begin{aligned} \boldsymbol{F}(\hat{\boldsymbol{r}}, \boldsymbol{k}) &\sim \int_\Omega \hat{\boldsymbol{r}} \times ((\boldsymbol{d} \cdot \boldsymbol{E}_0 \mathrm{e}^{-\mathrm{i}\boldsymbol{k}\cdot\boldsymbol{x}}) \hat{\boldsymbol{d}} \times \hat{\boldsymbol{r}}) \mathrm{e}^{\mathrm{i}k\hat{\boldsymbol{r}}\cdot\boldsymbol{x}} \, \mathrm{dV}_{\boldsymbol{x}} \\ &= \hat{\boldsymbol{r}} \times \int_\Omega \boldsymbol{\Gamma} \boldsymbol{E}_0 \mathrm{e}^{-\mathrm{i}(\boldsymbol{k} - k\hat{\boldsymbol{r}})\cdot\boldsymbol{x}} \, \mathrm{dV}_{\boldsymbol{x}} \times \hat{\boldsymbol{r}}. \end{aligned} \tag{4.3}$$

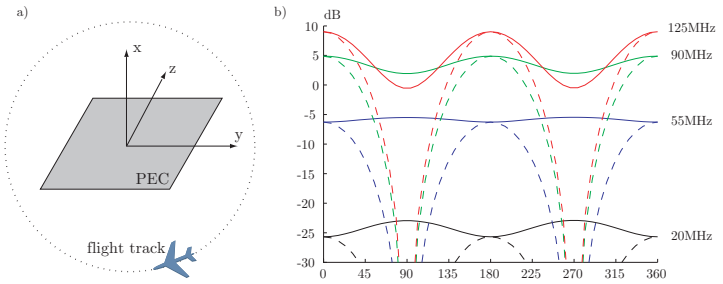

Figure 5: Mono-static scattering by a $1\,\mathrm{m} \times 1\,\mathrm{m}$ PEC plate for the frequencies $20, 55, 90, 125\,\mathrm{MHz}$. The vertical (TE) and horizontal (TM) cases are given by the solid and dashed curves, respectively.

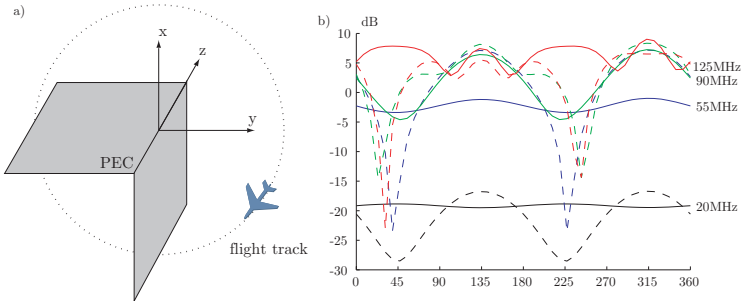

Figure 6: Mono-static scattering by a $(1+1)\,\mathrm{m} \times 1\,\mathrm{m}$ PEC wedge for the frequencies $20, 55, 90, 125\,\mathrm{MHz}$. The vertical (TE) and horizontal (TM) cases are given by the solid and dashed curves, respectively.

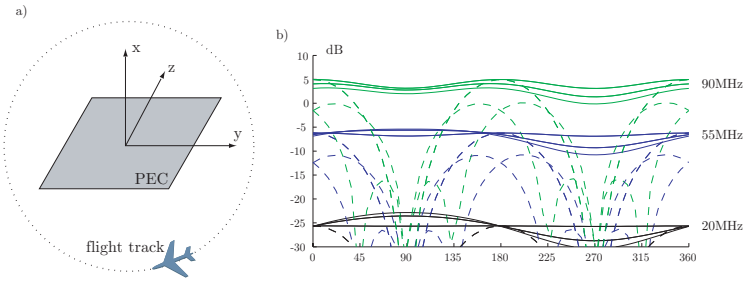

Figure 7: Bi-static scattering by a $(1+1)\,\mathrm{m} \times 1\,\mathrm{m}$ PEC plate for the frequencies $20, 55, 90\,\mathrm{MHz}$. The different curves correspond to illuminating wave field from $0°, 45°, 90°, 135°$, and $180°$. The vertical (TE) and horizontal (TM) cases are given by the solid and dashed curves, respectively.

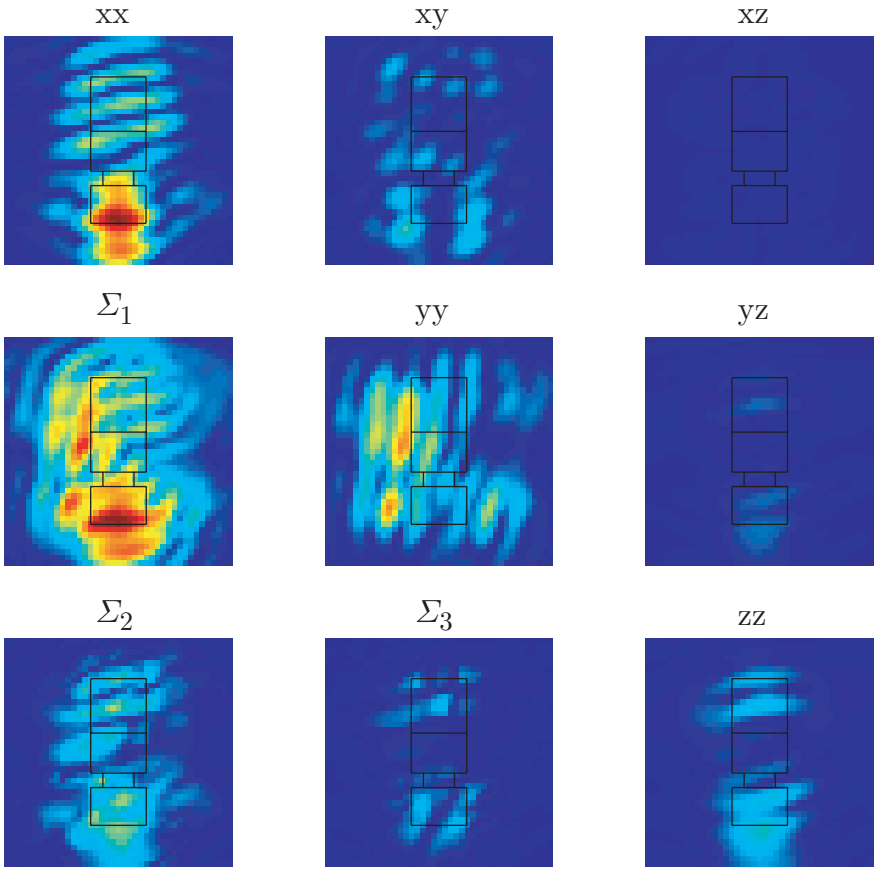

Figure 8: Dyadic SAR images from a combined vertically and horizontally polarized case and a flight track given by $\theta_o = 60°$ and $100° \leq \phi \leq 350°$. The horizontal polarization giving the xy-subspace dominates the image. The xx- and yy-components comes from the y- and x-directions, respectively. The corresponding SVD images are depicted in the lower triangular part of the matrix.

The dipole moments are represented by a matrix or dyad $\mathbf{\Gamma}$, *i.e.*, $\mathbf{\Gamma}\boldsymbol{E}_0 = \boldsymbol{d} \cdot \boldsymbol{E}_0\hat{\boldsymbol{d}}$, with the interpretation of three dipole moments given by the eigenvalues of $\mathbf{\Gamma}$ and the corresponding eigenvectors.

Due to the dyadic product between the anisotropic reflectivity and the illuminating wave field, the simple Fourier transform relation between the reflectivity and the far-field pattern is no longer valid. However, it is possible to use a least-squares inversion to approximate the anisotropic reflectivity. Define an error functional as the least-squares difference between the given (measured) far-field pattern $\boldsymbol{F}(\hat{\boldsymbol{r}}, \boldsymbol{k}) = \boldsymbol{F}(\tau, k)$ and a calculated far-field pattern $\boldsymbol{F}_\gamma(\hat{\boldsymbol{r}}, \hat{\boldsymbol{k}}, k) = \boldsymbol{F}_\gamma(\tau, k)$ that corresponds to the reflectivity $\gamma(\boldsymbol{x})$. The least-squares functional is given by the least-squares integral over the flight path, *i.e.*,

$$\mathcal{J}[\gamma] = \int_0^\Upsilon \int_{k_1}^{k_2} \psi(\tau, k) |\boldsymbol{F}_\gamma(\tau, k) - \boldsymbol{F}(\tau, k)|^2 \, \mathrm{d}k \, \mathrm{d}\tau, \tag{4.4}$$

where $\psi(\tau,k)$ is a suitable weight function. For multi-static data, a summation over the measurements is included in (4.4), *i.e.*, $\sum_{n=1}^{N}\sum_{m=1}^{M_n}$. A gradient based optimization algorithm such as the conjugate gradient algorithm can be used to find the reflectivity that minimizes (4.4).

Perturb the reflectivity γ as $\gamma(\boldsymbol{x}) \to \gamma_0(\boldsymbol{x}) + \delta\gamma'(\boldsymbol{x})$. The corresponding far-field pattern is perturbed as $\boldsymbol{F}_{\gamma_0+\delta\gamma'} = \boldsymbol{F}_{\gamma_0} + \delta\boldsymbol{F}_{\gamma'}$, where $\boldsymbol{F}_{\gamma'}$ is the far-field pattern of the reflectivity $\gamma'(\boldsymbol{x})$. The least-squares functional is linearized as

$$\begin{aligned}\mathcal{J}[\gamma_0+\delta\gamma'] &= \mathcal{J}[\gamma_0] \\ &\quad + \delta 2\,\mathrm{Re}\int_0^{\Upsilon}\int_{k_1}^{k_2} \psi(\tau,k)\boldsymbol{F}_{\gamma'}(\tau,k)\cdot\big(\boldsymbol{F}_{\gamma}(\tau,k)-\boldsymbol{F}(\tau,k)\big)^*\,\mathrm{d}k\,\mathrm{d}\tau + \mathrm{O}(\delta^2). \quad (4.5)\end{aligned}$$

The far-field pattern of a scalar reflectivity $\gamma(\boldsymbol{x})$ and an illuminating wave field

$$\boldsymbol{E}(\boldsymbol{x},\tau,k) = \boldsymbol{E}(\boldsymbol{x},\hat{\boldsymbol{k}}(\tau),k) = \boldsymbol{E}_0(\tau)\mathrm{e}^{-\mathrm{i}\boldsymbol{k}\cdot\boldsymbol{x}} \quad (4.6)$$

is

$$\boldsymbol{F}_{\gamma}(\tau) = \boldsymbol{F}_{\gamma}(\hat{\boldsymbol{r}}(\tau),\boldsymbol{k}(\tau)) = \hat{\boldsymbol{r}}\times\int_{\Omega}\boldsymbol{\Gamma}\boldsymbol{E}_0\mathrm{e}^{-\mathrm{i}(\boldsymbol{k}-k\hat{\boldsymbol{r}})\cdot\boldsymbol{x}}\,\mathrm{dV}_{\boldsymbol{x}}\times\hat{\boldsymbol{r}}. \quad (4.7)$$

The adjoint field to (3.1) is used to determine the gradient. The adjoint field is given by

$$\widetilde{\boldsymbol{E}}(\boldsymbol{x},\tau,k) = \widetilde{\boldsymbol{E}}(\boldsymbol{x},\hat{\boldsymbol{r}}(\tau),k) = \psi(\tau,k)\big(\boldsymbol{F}_{\gamma}(\tau)-\boldsymbol{F}(\tau)\big)^*\mathrm{e}^{-\mathrm{i}k\hat{\boldsymbol{r}}\cdot\boldsymbol{x}}. \quad (4.8)$$

The product between the perturbed illuminating field and the adjoint field integrated over wavenumber and flight path is

$$\begin{aligned}&\mathrm{Re}\int_{\Omega}\int_0^{\Upsilon}\int_{k_1}^{k_2}\widetilde{\boldsymbol{E}}(\boldsymbol{x},\tau,k)\cdot\boldsymbol{\Gamma}'(\boldsymbol{x})\boldsymbol{E}(\boldsymbol{x},\tau,k)\,\mathrm{d}k\,\mathrm{d}\tau\,\mathrm{dV}_{\boldsymbol{x}} \\ &\quad= \mathrm{Re}\int_{\Omega}\int_0^{\Upsilon}\int_{k_1}^{k_2}\hat{\boldsymbol{r}}\times(\widetilde{\boldsymbol{E}}(\boldsymbol{x},\tau,k)\times\hat{\boldsymbol{r}})\cdot\boldsymbol{\Gamma}'(\boldsymbol{x})\boldsymbol{E}(\boldsymbol{x},\tau,k)\,\mathrm{d}k\,\mathrm{d}\tau\,\mathrm{dV}_{\boldsymbol{x}} \\ &\quad= \mathrm{Re}\int_{\Omega}\int_0^{\Upsilon}\int_{k_1}^{k_2}\widetilde{\boldsymbol{E}}(\boldsymbol{x},\tau,k)\cdot\big((\hat{\boldsymbol{r}}\times(\boldsymbol{\Gamma}'(\boldsymbol{x})\boldsymbol{E}(\boldsymbol{x},\tau,k))\times\hat{\boldsymbol{r}}\big)\,\mathrm{d}k\,\mathrm{d}\tau\,\mathrm{dV}_{\boldsymbol{x}} \\ &= \mathrm{Re}\int_0^{\Upsilon}\int_{k_1}^{k_2}\psi(\tau,k)\big(\boldsymbol{F}_{\gamma}(\tau,k)-\boldsymbol{F}(\tau,k)\big)^*\cdot\int_{\Omega}\boldsymbol{E}_0(\boldsymbol{k})\mathrm{e}^{-\mathrm{i}(k\hat{\boldsymbol{r}}-\boldsymbol{k})\cdot\boldsymbol{x}}\gamma'(\boldsymbol{x})\,\mathrm{dV}_{\boldsymbol{x}}\,\mathrm{d}k\,\mathrm{d}\tau \\ &\quad= \mathrm{Re}\int_0^{\Upsilon}\int_{k_1}^{k_2}\psi(\tau,k)\big(\boldsymbol{F}_{\gamma}(\tau,k)-\boldsymbol{F}(\tau,k)\big)^*\cdot\boldsymbol{F}_{\gamma'}(\tau,k)\,\mathrm{d}k\,\mathrm{d}\tau \quad (4.9)\end{aligned}$$

where, the identities $\widetilde{\boldsymbol{E}} = \hat{\boldsymbol{r}}\times(\widetilde{\boldsymbol{E}}\times\hat{\boldsymbol{r}})$ and

$$\big(\hat{\boldsymbol{r}}\times(\boldsymbol{F}\times\hat{\boldsymbol{r}})\big)\cdot\boldsymbol{E} = \boldsymbol{F}\cdot\big((\hat{\boldsymbol{r}}\times\boldsymbol{E})\times\hat{\boldsymbol{r}}\big) \quad (4.10)$$

are used. Hence, to minimize the least-squares functional the perturbation should be made in the direction such that (4.9) is maximized. Rewrite the vector matrix products in the first term of (4.9) as

$$\widetilde{\boldsymbol{E}}\cdot\boldsymbol{\Gamma}'\boldsymbol{E} = \sum_{i=1}^{3}\sum_{j=1}^{3}\widetilde{E}_i\Gamma'_{ij}E_j = \sum_{i=1}^{3}\sum_{j=1}^{3}\Gamma'_{ij}\widetilde{E}_iE_j = \boldsymbol{\Gamma}'\widetilde{\boldsymbol{E}}\boldsymbol{E}, \quad (4.11)$$

where $\widetilde{\boldsymbol{E}}\boldsymbol{E}$ is the dyadic product between the vectors $\widetilde{\boldsymbol{E}}$ and $\boldsymbol{E}$. This gives the gradients

$$\mathbf{G}_\Gamma(\boldsymbol{x}) = \int_0^\Upsilon \int_{k_1}^{k_2} \boldsymbol{E}^*(\boldsymbol{x},\tau,k)\widetilde{\boldsymbol{E}}^*(\boldsymbol{x},\tau,k)\,\mathrm{d}k\,\mathrm{d}\tau. \tag{4.12}$$

As in the point scattering model, the update direction is identified with the SAR image, *i.e.*, $\mathbf{\Gamma}(\boldsymbol{x}) = \mathbf{G}_\Gamma(\boldsymbol{x})$. This image consists of the images of each matrix element of $\mathbf{\Gamma}(\boldsymbol{x})$, *i.e.*, Γ_{ij} for $i,j = 1,2,3$ or $i,j = \mathrm{x},\mathrm{y},\mathrm{z}$, see *e.g.*, Figure 8. An eigenvalue decomposition or singular value decomposition of the matrix $\mathbf{\Gamma}(\boldsymbol{x})$ can be used to obtain coordinate independent images, see *e.g.*, Figure 8. In the free space case, the explicit expressions for the illuminating field and the time reversed field gives

$$\begin{aligned}\mathbf{\Gamma}(\boldsymbol{x}) &= \int_0^\Upsilon \int_{k_1}^{k_2} \boldsymbol{E}^*(\boldsymbol{x},\tau,k)\widetilde{\boldsymbol{E}}^*(\boldsymbol{x},\tau,k)\,\mathrm{d}k\,\mathrm{d}\tau \\ &= \int_0^\Upsilon \int_{k_1}^{k_2} \psi(\tau,k)\boldsymbol{E}_0^*(\tau,k)\mathrm{e}^{\mathrm{i}k\hat{\boldsymbol{k}}\cdot\boldsymbol{x}}\boldsymbol{F}(\tau,k)\mathrm{e}^{-\mathrm{i}k\hat{\boldsymbol{r}}\cdot\boldsymbol{x}}\,\mathrm{d}k\,\mathrm{d}\tau \\ &= \int_0^\Upsilon \int_{k_1}^{k_2} \psi(\tau,k)\boldsymbol{E}_0^*(\tau,k)\boldsymbol{F}(\tau,k)\mathrm{e}^{\mathrm{i}k(\hat{\boldsymbol{k}}(\tau)-\hat{\boldsymbol{r}}(\tau))\cdot\boldsymbol{x}}\,\mathrm{d}k\,\mathrm{d}\tau. \end{aligned}\tag{4.13}$$

With multi-static data a summation over the measurements is added, *i.e.*,

$$\mathbf{\Gamma}(\boldsymbol{x}) = \sum_{n=1}^{N}\sum_{m=1}^{M_n} \int_0^{\Upsilon_n} \int_{k_1}^{k_2} \psi(\tau,k)\boldsymbol{E}_{0n}^*(\tau,k)\boldsymbol{F}_{mn}(\tau,k)\mathrm{e}^{\mathrm{i}k(\hat{\boldsymbol{k}}_n(\tau)-\hat{\boldsymbol{r}}_{mn}(\tau))\cdot\boldsymbol{x}}\,\mathrm{d}k\,\mathrm{d}\tau. \tag{4.14}$$

4.2 Dipole images of the FDTD vehicle

To illustrate the dipole scattering model or anisotropic scattering model FDTD simulated SAR data is used [16], see also Figure 3 and the discussion in Section 3.1.

In Figure 9, the singular value decomposed dipole images for a 90° flight track between 180° to 270° are shown. The images are given by a SVD of the reflection matrix. It is observed that the first singular value dominates the 180°, 240°, and 270° cases, *i.e.*, there is only one dominating scattering process in theses cases. However, in the 210° and 225° cases there are orthogonal scattering processes in the front and at the side of the vehicle. Notice the similarity with the directionally decomposed images in Figure 3.

The dipole images and the point images are compared for the 180° to 270° cases in Figure 10. Here, it is seen that the interference of the point images are eliminated in the dipole images. Moreover, the physics of the scattering process is included in the dipole images by the short line depicting the dipole directions and lengths.

In Figure 11, mono-static SAR images from the point scatter model (top row) and dipole scatter model (bottom row) for the aperture angles $40°, 80°, 120°, 160°$ are compared. It is noted that the point scatter model and dipole scatter model give similar results for small to moderate aperture angles. This is also expected from the theory since one polarization dominates the wave propagation for these cases. As the aperture increases the polarization can not be neglected. At a 90° aperture orthogonal polarizations are used in the horizontally polarized case.

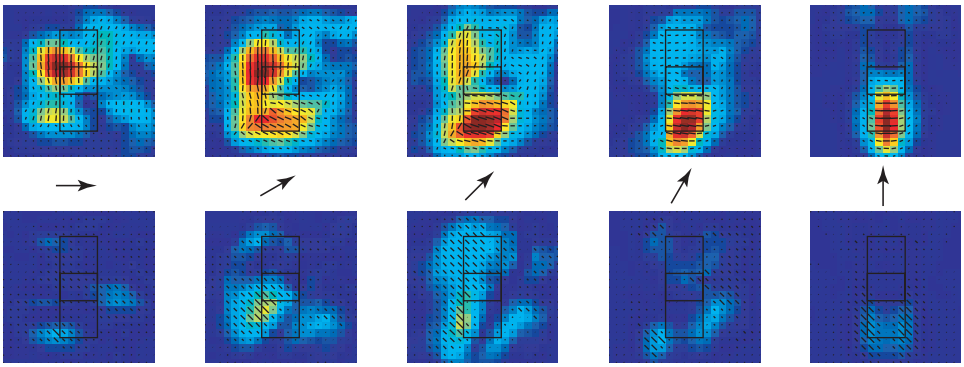

Figure 9: SAR images with a with an anisotropic source. The first and second singular values are shown in the first and second row, respectively. The flight track is between 180° to 270° with an average illumination indicated by the arrows.

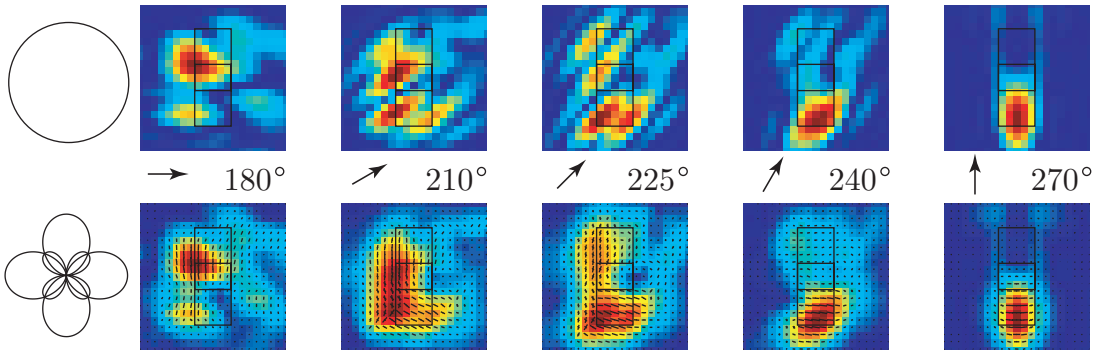

Figure 10: Comparison between the SAR images with a point source (top row) and SAR images with an anisotropic source (bottom row). The flight track is between 180° to 270° with an average illumination indicated by the arrows.

In Figure 12, a comparison between bi-static SAR images for the point scatter model and dipole scatter model is shown. The vehicle is illuminated with a fixed horizontal wave from an elevation of 75° and azimuth indicated by the arrow. The field is received on a circular path at elevation 65°. The dipole image has only one singular value for a bi-static setup with a fixed illumination.

4.3 Horizontal and vertical polarization

Consider a bi-static flight track in spherical coordinates $\{\theta_{\rm i}, \phi_{\rm i}\}$ and $\{\theta_{\rm o}, \phi_{\rm o}\}$. With a horizontally polarized antenna, the transmitted and received wave is of the form $\hat{\boldsymbol{\phi}}_{\rm i}\hat{\boldsymbol{\phi}}_{\rm o}$. This gives the dyadic product of the form

$$\hat{\boldsymbol{\phi}}_{\rm i}\hat{\boldsymbol{\phi}}_{\rm o} = \begin{pmatrix} \sin\phi_{\rm i}\sin\phi_{\rm o} & -\sin\phi_{\rm i}\cos\phi_{\rm o} & 0 \\ -\sin\phi_{\rm i}\cos\phi_{\rm o} & \cos\phi_{\rm i}\cos\phi_{\rm o} & 0 \\ 0 & 0 & 0 \end{pmatrix} \tag{4.15}$$

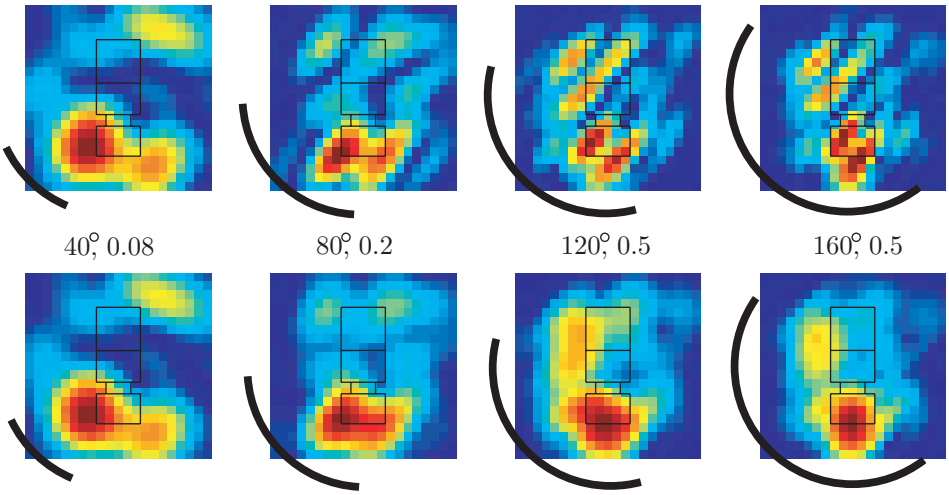

Figure 11: Comparison between mono-static SAR images from the point scatter model (top row) and dipole scatter model (bottom row) for the aperture angles $40°, 80°, 120°, 160°$ as indicated by the circular arcs. The vehicle is illuminated with a horizontal wave from an elevation of $60°$.

Here it is observed that the dyad is independent of the θ_0 angle. Moreover, it is only the horizontal part, *i.e.*, the $\{x, y\}$-subspace, of the dyad that is non-zero.

With a vertically polarized antenna, the transmitted and received wave is if the form $\hat{\boldsymbol{\theta}}_\mathrm{i}\hat{\boldsymbol{\theta}}_\mathrm{o}$. This gives the dyadic product

$$\hat{\boldsymbol{\theta}}_\mathrm{i}\hat{\boldsymbol{\theta}}_\mathrm{o} = \begin{pmatrix} \cos\phi_\mathrm{i}\cos\theta_\mathrm{i}\cos\phi_\mathrm{o}\cos\theta_\mathrm{o} & \cos\phi_\mathrm{i}\cos\theta_\mathrm{i}\cos\phi_\mathrm{o}\sin\theta_\mathrm{o} & -\cos\phi_\mathrm{i}\cos\theta_\mathrm{i}\sin\theta_\mathrm{o} \\ \sin\phi_\mathrm{i}\cos\theta_\mathrm{i}\cos\phi_\mathrm{o}\cos\theta_\mathrm{o} & \sin\phi_\mathrm{i}\cos\theta_\mathrm{i}\cos\phi_\mathrm{o}\sin\theta_\mathrm{o} & -\sin\phi_\mathrm{i}\cos\theta_\mathrm{i}\sin\theta_\mathrm{o} \\ -\sin\theta_\mathrm{i}\cos\phi_\mathrm{o}\cos\theta_\mathrm{o} & -\sin\theta_\mathrm{i}\cos\phi_\mathrm{o}\sin\theta_\mathrm{o} & \sin\theta_\mathrm{i}\sin\theta_\mathrm{o} \end{pmatrix} \tag{4.16}$$

Here, all elements are in general non-zero. However, for low elevation angles, *i.e.*, $\theta_0 \approx 90°$, the dyad is dominated by the vertical component, $\hat{\boldsymbol{z}}\hat{\boldsymbol{z}}$. It is also observed that this component is independent of the ϕ-component.

In Figure 13, SAR images of the FDTD vehicle are shown in the point and dipole approximation for a $\theta_\mathrm{o} = 60°$ and $100° \leq \phi \leq 350°$ flight track with either a vertically or a horizontally polarized antenna. For the horizontal polarization, it is observed that the interference behavior is reduced with the dipole model. In the vertically polarized case, it is hard to observe any differences between the point and dipole approximations. However, the vertically polarized case is not affected by the point scatter interference to the same degree as the horizontally polarized case. Due to the large aperture angle, 250°, and the erroneous treatment of the ground interaction there is an interference behavior between the scattering from the 180° ambiguity.

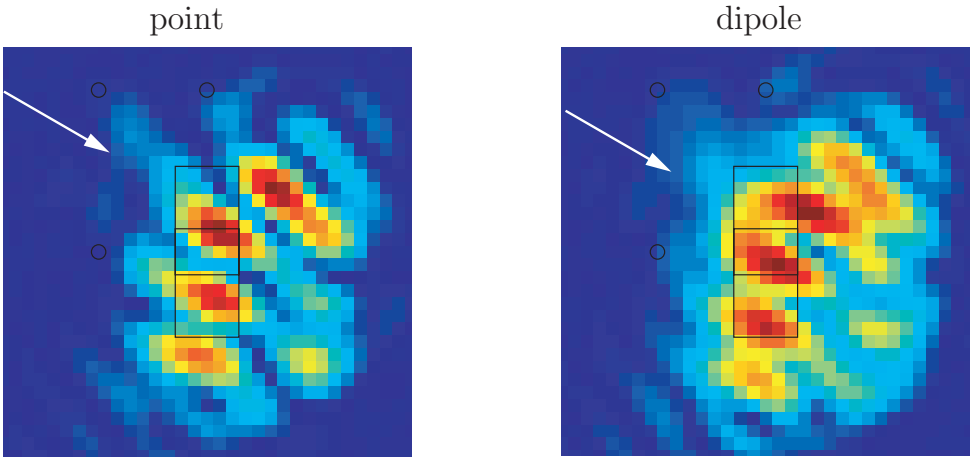

Figure 12: Comparison between bi-static SAR images for the point scatter model and dipole scatter model. The vehicle is illuminated with a fixed horizontal wave from an elevation of 75° and azimuth indicated by the arrow. The field is received on a circular path at elevation 65°.

5 Resolution

It is easy to have an intuitive understanding of the resolution of an imaging systems as the systems capability to resolve different object. Unfortunately, there are several types of resolution, *e.g.*, in SAR it is common to talk about angular resolution, azimuth resolution, range resolution, resolution cell, slant altitude resolution, geometrical resolution, and radiometric resolution [7], hence it is necessary give definitions for the type of resolution that is used. In mono-static SAR with a moderate aperture angle, the range resolutions is given by the bandwidth, *i.e.*, $c_0/2/\Delta f$. The resolution of the transverse direction is given by the aperture angle and the frequency [7]. In realistic systems, the resolution depends in the signal to noise ratio (SNR), *e.g.*, the ground reflection gives a large noise level in bi-static SAR, see Figure 14.

Due to the vector nature of the EM field the resolution also depends on the polarization. For a low elevation angle and a vertically polarized antenna the image is given by a Fourier transform with the spectral coverage given by (3.5), see Figure 2. For multi-static cases the SAR image in (4.14) is used. For vertically polarized antennas it is sufficient to consider the spectral coverage of the image. From (4.14) the spectral coverage is given by

$$\sum_{n=1}^{N}\sum_{m=1}^{M_n} k(\hat{\boldsymbol{k}}_n(\tau) - \hat{\boldsymbol{r}}_{mn}(\tau)) \tag{5.1}$$

where $0 \leq \tau \leq \Upsilon_n$ and $k_1 \leq k \leq k_2$. In Figure 15, the case with four fixed illuminations at azimuth angles $0°, 90°, 180°$, and $270°$ and a circular receiving flight path is shown. The elevation angle is fix at 90°, other elevation angles give a scaling with $\sin\theta$ in the spectral domain. In the figure, it is observed that the 360° and 180°

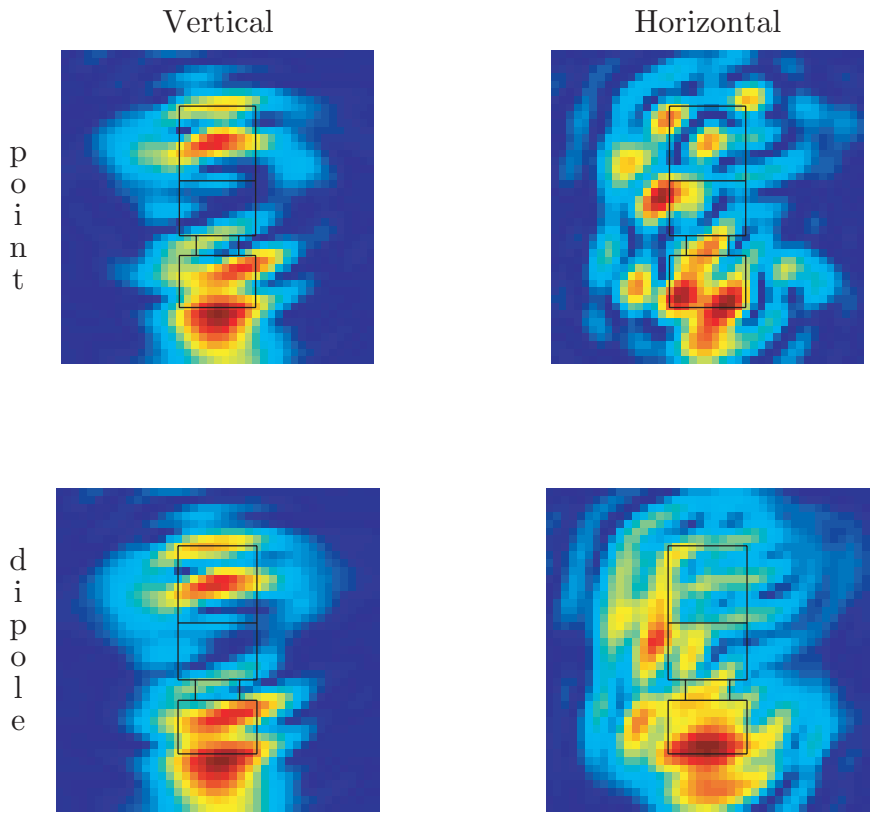

Figure 13: Comparison between point scatter images and dipole scatter images for a vertical and horizontal polarized case.

cases has a complete angular spectral coverage, they only differ for small k values. The spectral coverage of the 90° case is half the unit circle. However, observe that 360° and 180° cases require simultaneous reception of more than one signal. In the 90° case, only one signal is received for each position.

In Figure 16, the spectral coverage with four transmitting and receiving paths are shown. The flight paths are gives by $-\Delta\phi/2 \leq \phi - n\pi/2 \leq \Delta\phi/2$ for $n = 0, 1, 2, 3$ and $\Delta\phi = 80°, 40°$. Each plane transmits one wave and receives three separate waves, *i.e.*, the mono-static wave and the bi-static waves from its closes neighbors. The wave in the forward direction gives only depths information. The mono-static part of the 80° case gives almost complete angular spectral coverage, a 90° would be equivalent to a circular flight path surrounding the object. In addition to the mono-static part, there is a bi-static contribution. This part has smaller spectral coverage in the radial direction.

To get a basic understanding of the resolving capabilities of a SAR imaging system the image of a small PEC sphere is considered. The scattering properties of a sphere are well known and given by analytic expressions. For a sufficiently small

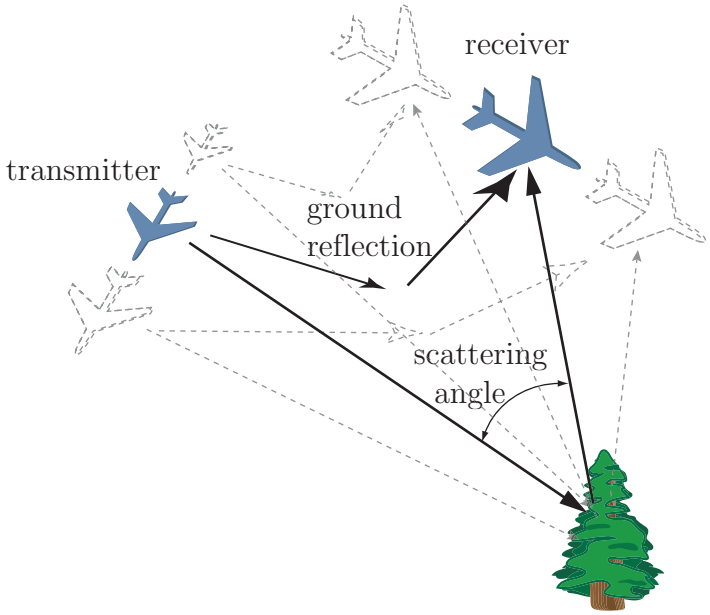

Figure 14: Setup for bi-static SAR. The received signal is given by the scattering from the object (or objects) and the reflection from the ground.

sphere with radius a, the scattering matrix is

$$S(\boldsymbol{k}, \hat{\boldsymbol{r}}) = k^3 a^3 \begin{pmatrix} \cos\theta - \frac{1}{2} & 0 \\ 0 & 1 - \frac{\cos\theta}{2} \end{pmatrix}, \tag{5.2}$$

where θ is the angle between the incident plane wave $\boldsymbol{k}$ and the scattering direction $\hat{\boldsymbol{r}}$, see [12]. For low elevation angles, the terms $\cos\theta - \frac{1}{2}$ and $1 - \frac{\cos\theta}{2}$ correspond to horizontally and vertically polarized antennas, respectively. The scattering dyad can be interpreted as a sum of an electric dipole part and a magnetic dipole part. The scattering is dominated by the electric part that has twice the amplitude as the magnetic part. The mono-static case gives $\frac{3k^3a^3}{2}$. Observe that there are no cross coupling term in the scattering matrix.

For a mono-static flight path parametrized by $\theta = \theta_0$ and $|\phi| \leq \phi_0/2$ the dipole SAR image

$$\begin{aligned} \boldsymbol{\Gamma}(\boldsymbol{x}) &\sim \frac{3a^3}{2} \int_{-\phi_0/2}^{\phi_0/2} \int_{k_0-\Delta k/2}^{k_0+\Delta k/2} \boldsymbol{E}_0 \boldsymbol{E}_0^* \mathrm{e}^{2\mathrm{i}k\hat{\boldsymbol{k}}\cdot\boldsymbol{x}} \,\mathrm{d}k \,\mathrm{d}\phi \\ &= \frac{3a^3}{2} \int_{-\phi_0/2}^{\phi_0/2} \boldsymbol{E}_0 \boldsymbol{E}_0^* \mathrm{e}^{2\mathrm{i}k_0\boldsymbol{x}\cdot\hat{\boldsymbol{k}}} \frac{\sin(\Delta k \hat{\boldsymbol{k}}\cdot\boldsymbol{x})}{\hat{\boldsymbol{k}}\cdot\boldsymbol{x}} \,\mathrm{d}\phi \end{aligned} \tag{5.3}$$

where the dyadic product is given by (4.15) and (4.16) in the horizontally and vertically polarized cases, respectively. Cuts along the x-direction and y-direction is seen in Figure 17. Plotting the image for the CARABAS-II frequencies, gives a spot size radius of approximately 1 m, see also [18]. Hence it is difficult to separate

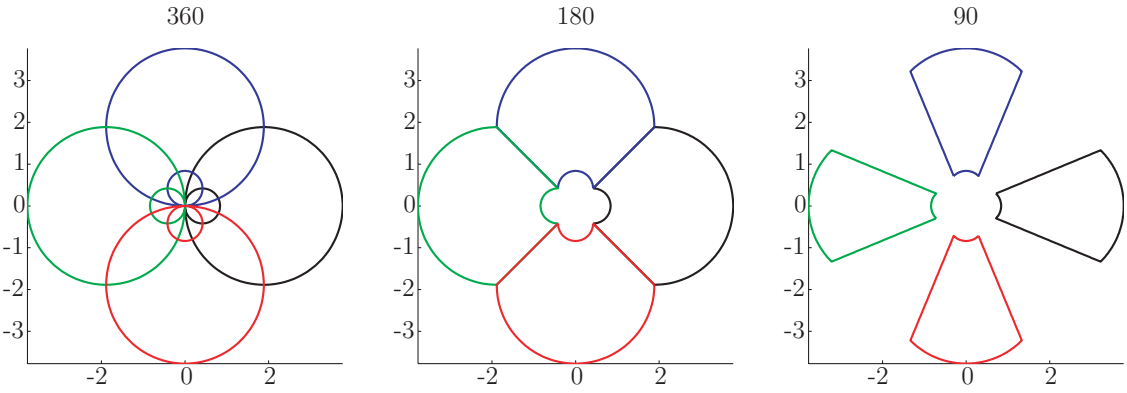

Figure 15: The spectral coverage for a multi-static setup with four separate illuminating waves from the azimuth angles $0°, 90°, 180°$, and $270°$ and a circular receiving flight path.

objects smaller than 1 m. However, the scattering properties of theses types of small objects can be very different, see *e.g.*, Figure 5.

For a bi-static setup the SAR image of the sphere is

$$\begin{aligned}\boldsymbol{\Gamma}(\boldsymbol{x}) &= \int_0^{\Upsilon}\int_{k_0-\Delta k/2}^{k_0+\Delta k/2} \boldsymbol{E}_0\boldsymbol{E}_0^* \mathrm{e}^{\mathrm{i}k(\hat{\boldsymbol{k}}-\hat{\boldsymbol{r}})\cdot\boldsymbol{x}}\,\mathrm{d}k\,\mathrm{d}\tau \\ &= 2\int_{-0}^{0} \boldsymbol{E}_0\mathbf{S}\boldsymbol{E}_0^* \mathrm{e}^{\mathrm{i}k_0\boldsymbol{x}\cdot(\hat{\boldsymbol{k}}-\hat{\boldsymbol{r}})}\frac{\sin(\Delta k(\hat{\boldsymbol{k}}-\hat{\boldsymbol{r}})\cdot\boldsymbol{x}/2)}{(\hat{\boldsymbol{k}}-\hat{\boldsymbol{r}})\cdot\boldsymbol{x}}\,\mathrm{d}\tau. \quad (5.4)\end{aligned}$$

The SAR images of a fixed illumination given by a horizontally polarized plane wave in the $\hat{\boldsymbol{k}} = \hat{\boldsymbol{x}}$ direction, *i.e.*,

$$\boldsymbol{E}(\boldsymbol{x},\tau,k) = E_0\hat{\boldsymbol{y}}\mathrm{e}^{-\mathrm{i}kx}, \quad (5.5)$$

and a horizontally polarized receiving antenna along the path $\theta_\mathrm{o} = 90°$, $\phi_0 - \Delta\phi/2 \leq \phi_\mathrm{o} \leq \phi_0 - \Delta\phi/2$ is shown in Figure 18. In the figure, it is seen that the resolution is comparable with the mono-static case, *cf.* with Figure 17, for the 180° case, *i.e.*, in the back-scattering direction. As the angle between the illumination and the reception decreases the resolution deteriorate. This is partly due to the scattering properties of the sphere, *i.e.*, the backscattering dominates and there is no scattering in 60°. However it is also due to the decreased resolution of the imaging system, see Figure 2. Notice that the resolution in the $\hat{\boldsymbol{x}}$ direction deteriorates much faster than the $\hat{\boldsymbol{y}}$ resolution, *cf.* with Figure 2. The corresponding case with vertically polarized antennas is shown in Figure 19. Here, it is also observed that the best resolution is obtained in the back direction. It is also observed that image is in general better than the horizontally polarized case, since the vector nature of the EM field can be neglected.

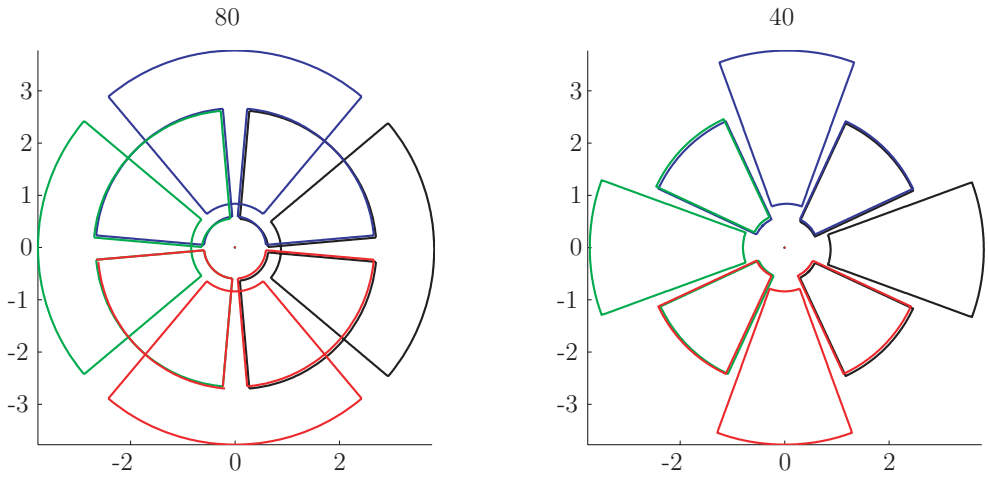

Figure 16: The spectral coverage with four transmitting and receiving paths given by $-\Delta\phi/2 \leq \phi - n\pi/2 \leq \Delta\phi/2$ for $n = 0, 1, 2, 3$ and $\Delta\phi = 80°, 40°$.

6 Non-linear inversion

As mentioned in Section 2.2, the SAR imaging problem can be formulated as a time-domain least-squares problem. The electromagnetic field consists of the electric and magnetic fields, *i.e.*, the electric field intensity $\boldsymbol{E}$, the magnetic field intensity $\boldsymbol{H}$, the electric flux density $\boldsymbol{D}$, and the magnetic flux density $\boldsymbol{B}$. The Maxwell equations govern the evolution of electromagnetic waves. The Maxwell equations are given by the Ampere's law and the Faraday's law. They are

$$\begin{cases} \partial_t \boldsymbol{D} - \nabla \times \boldsymbol{H} = \boldsymbol{0}, \\ \partial_t \boldsymbol{B} + \nabla \times \boldsymbol{E} = \boldsymbol{0}. \end{cases} \tag{6.1}$$

The interaction between electromagnetic waves and matter is modeled with a set of constitutive relations, *i.e.*, a relation between the flux densities $\{\boldsymbol{D}, \boldsymbol{B}\}$ and the field intensities $\{\boldsymbol{E}, \boldsymbol{H}\}$.

The least-squares inverse scattering formulation is based in minimizing the functional

$$\mathrm{J}[\epsilon] = \sum_{\text{measurements}} \int_0^{\Upsilon} \int_0^{T} |\boldsymbol{E}(\boldsymbol{r}(\tau), t) - \boldsymbol{E}^{(\mathrm{m})}(\boldsymbol{r}(\tau), t)|^2 \, \mathrm{d}t \, \mathrm{d}\tau \tag{6.2}$$

where $\boldsymbol{E}$ satisfies the Maxwell equations(6.1) with material parameters ϵ. The update directions are derived by a perturbation of the material parameters, *i.e.*, the constitutive relations [9]. The adjoint fields satisfy the Maxwell equations(6.1) and are solved backwards in time. To find the gradient with respect to the constitutive parameters ϵ, μ, and σ, the parameters are perturbed an amount δ, *i.e.*,

$$\begin{cases} \epsilon(\boldsymbol{x}) \to \epsilon(\boldsymbol{x}) + \delta\epsilon'(\boldsymbol{x}), \\ \mu(\boldsymbol{x}) \to \mu(\boldsymbol{x}) + \delta\mu'(\boldsymbol{x}), \\ \sigma(\boldsymbol{x}) \to \sigma(\boldsymbol{x}) + \delta\sigma'(\boldsymbol{x}). \end{cases}$$

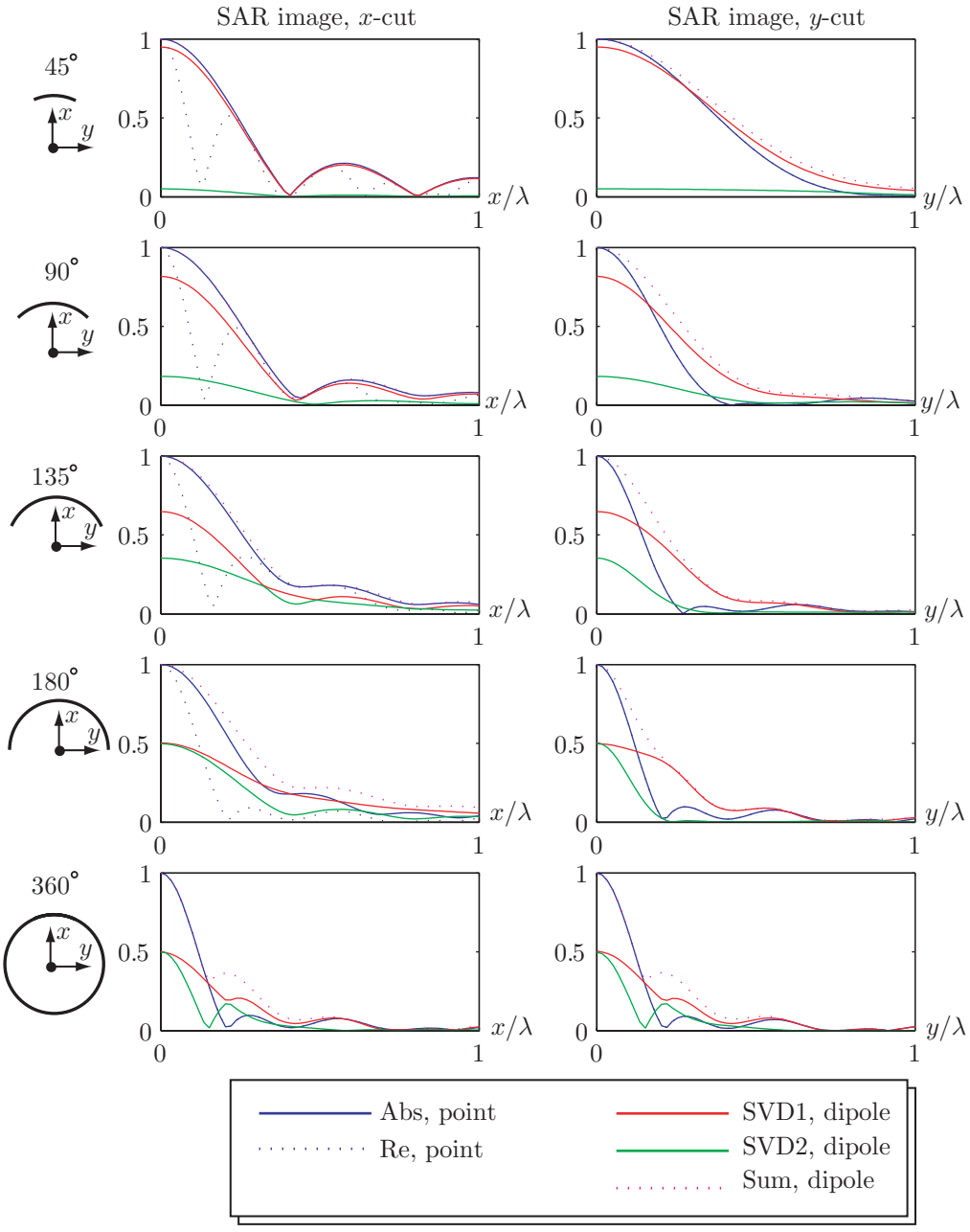

Figure 17: Range and transverse cuts through point and dipole images of a small PEC sphere for different aperture angles.

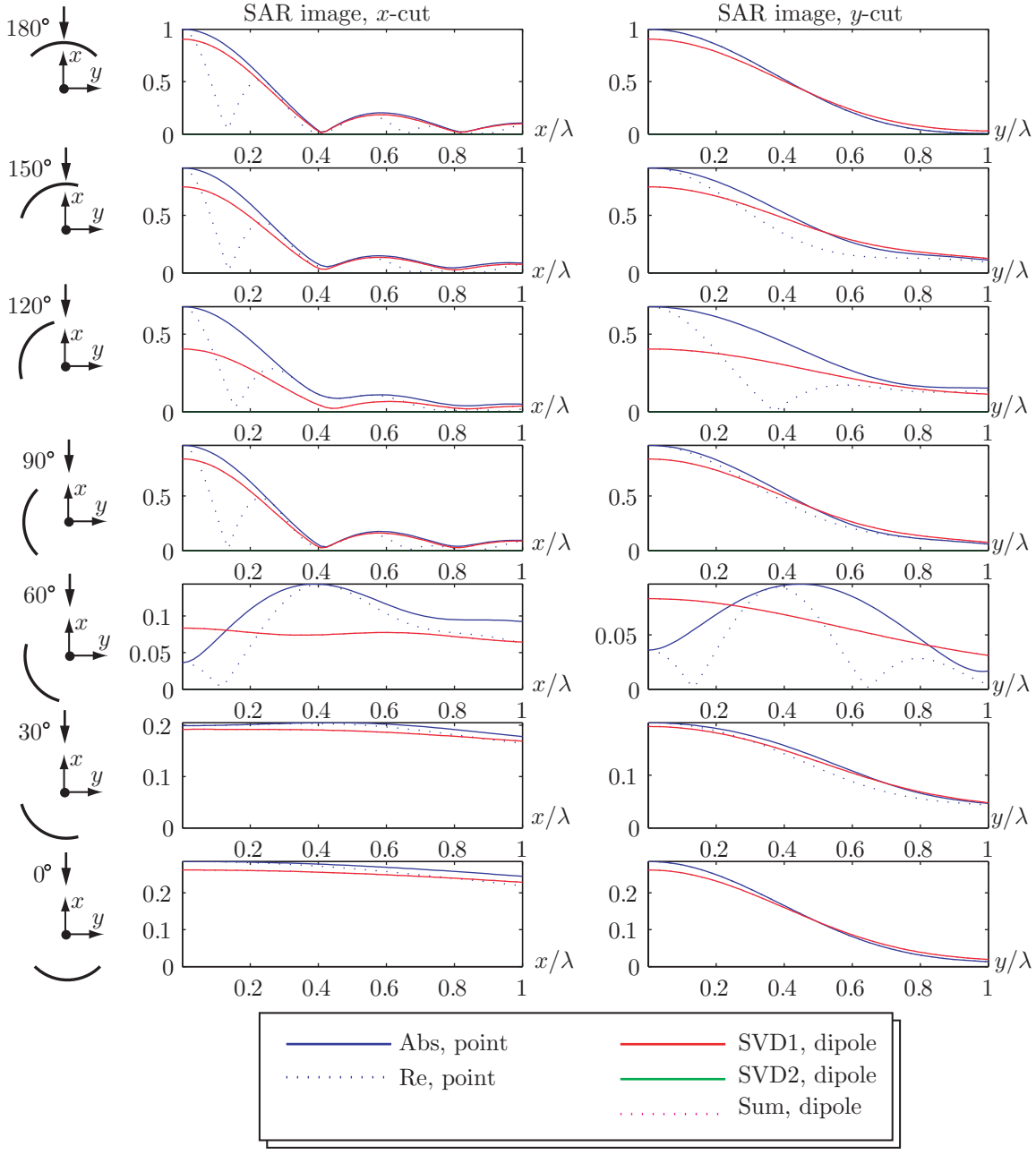

Figure 18: Range and transverse cuts through point and dipole images of a small PEC sphere for different scattering angles and a horizontally polarized antenna.

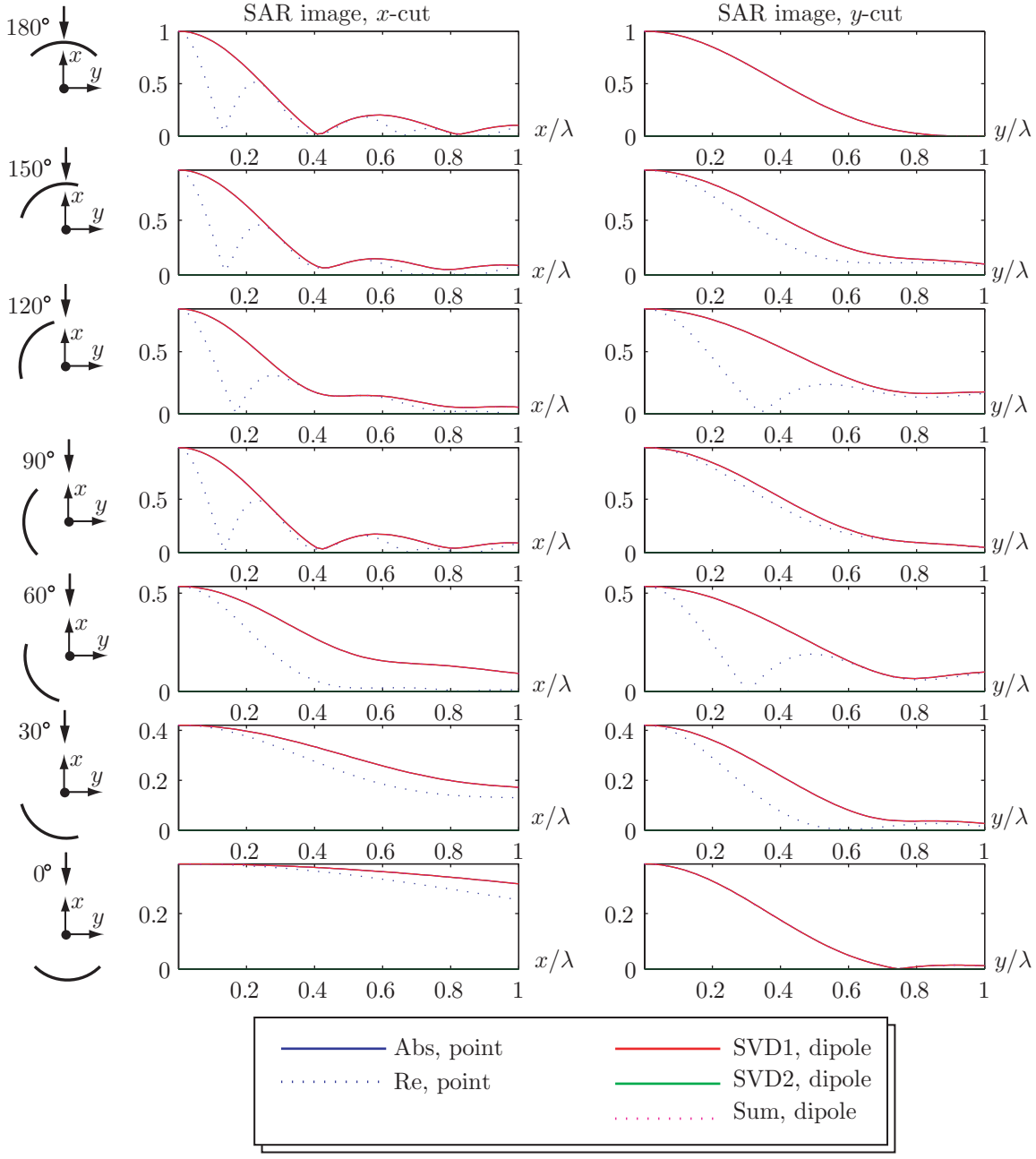

Figure 19: Range and transverse cuts through point and dipole SAR images of a small PEC sphere for different scattering angles and a vertically polarized antenna.

The corresponding fields $\boldsymbol{E}$ and $\boldsymbol{H}$ in are perturbed as

$$\begin{cases} \boldsymbol{E} \to \boldsymbol{E} + \delta \boldsymbol{E}' + \mathrm{O}(\delta^2), \\ \boldsymbol{H} \to \boldsymbol{H} + \delta \boldsymbol{H}' + \mathrm{O}(\delta^2), \end{cases} \tag{6.3}$$

where $\mathrm{O}(\delta^2)$ is a term of the size δ^2, *i.e.*, $\| \mathrm{O}(\delta^2) \| \leq C\delta^2$ as $\delta \to 0$. The gradients of the misfit functional with respect to the parameters ϵ, μ, and σ are found by calculating the increment of the misfit functional to the first order, *i.e.*,

$$\begin{aligned} \mathcal{J}'[\epsilon, \mu, \sigma] =& \lim_{\delta \to 0} \frac{\mathcal{J}[\epsilon + \delta\epsilon', \mu + \delta\mu', \sigma + \delta\sigma'] - \mathcal{J}[\epsilon, \mu, \sigma]}{\delta} \\ =& 4 \sum_{\text{measurements}} \int_0^{\Upsilon} \int_0^T \Phi \boldsymbol{E}' \cdot (\boldsymbol{E} - \boldsymbol{E}^{(\mathrm{m})}) \, \mathrm{d}t \, \mathrm{d}\tau. \end{aligned} \tag{6.4}$$

The first order perturbations of the calculated fields $\boldsymbol{E}'$ and $\boldsymbol{H}'$ satisfy the Maxwell equations

$$\begin{cases} \epsilon \partial_t \boldsymbol{E}' - \nabla \times \boldsymbol{H}' + \sigma \boldsymbol{E}' = -\epsilon' \partial_t \boldsymbol{E} - \sigma' \boldsymbol{E}, \\ \mu \partial_t \boldsymbol{H}' + \nabla \times \boldsymbol{E}' = -\mu' \partial_t \boldsymbol{H}, \end{cases} \tag{6.5}$$

where the induced sources are given by the unperturbed fields. The initial values and boundary values are $\boldsymbol{E}'(\boldsymbol{x}, 0) = \boldsymbol{H}'(\boldsymbol{x}, 0) = \boldsymbol{0}$ and no illuminating field.

The gradients are determined by the solution of an adjoint problem. The adjoint fields $\{\widetilde{\boldsymbol{E}}, \widetilde{\boldsymbol{H}}\}$ are determined by the Maxwell equations solved backwards in time with quiescent initial conditions and an incident wave field far from the object.

$$\begin{cases} \partial_t \epsilon \widetilde{\boldsymbol{E}} - \nabla \times \widetilde{\boldsymbol{H}} = -\widetilde{\boldsymbol{J}}, \\ \partial_t \widetilde{\boldsymbol{H}} + \nabla \times \widetilde{\boldsymbol{E}} = \boldsymbol{0} \end{cases} \tag{6.6}$$

This adjoint equation is solved backwards in time, from $t = T$ to $t = 0$, with quiescent initial values

$$\widetilde{\boldsymbol{E}}(\boldsymbol{x}, T) = \widetilde{\boldsymbol{H}}(\boldsymbol{x}, T) = \boldsymbol{0}.$$

At the receiving antenna, the adjoint current density is given by the difference between the calculated output field and the given output field, *i.e.*,

$$\widetilde{\boldsymbol{J}}(\boldsymbol{x}, t) = \boldsymbol{E}(\boldsymbol{x}, t) - \boldsymbol{E}^{(\mathrm{m})}(\boldsymbol{x}, t) \quad \text{for} \quad \boldsymbol{x} \in \Omega, \tag{6.7}$$

The adjoint equation is essentially the original equation (the conductivity changes sign) solved backwards in time with a current density depending on the difference between the calculated output and the given output fields.

Cross multiply the fields of the perturbed equation with the fields of the adjoint problem, add and collect terms to get

$$\begin{aligned} \boldsymbol{E}' \cdot \widetilde{\boldsymbol{J}} + \partial_t \left(\frac{\epsilon}{2} \boldsymbol{E}' \cdot \widetilde{\boldsymbol{E}} + \frac{\mu}{2} \boldsymbol{H}' \cdot \widetilde{\boldsymbol{E}} \right) + \nabla \cdot (\widetilde{\boldsymbol{E}} \times \boldsymbol{H}' + \boldsymbol{E}' \times \widetilde{\boldsymbol{E}}) \\ = -\epsilon' \widetilde{\boldsymbol{E}} \cdot \partial_t \boldsymbol{E} - \mu' \widetilde{\boldsymbol{E}} \cdot \partial_t \boldsymbol{H} - \sigma' \widetilde{\boldsymbol{E}} \cdot \boldsymbol{E}. \end{aligned}$$

Integrate this relation over time $[0,T]$ and space Ω. The second term vanishes according to the initial values of the perturbed and adjoint problems, and the third term gives an integral over the boundary that vanish if the radius of the region is sufficiently large such that the field have not reached surface. , *i.e.*,

$$\int_0^\Upsilon \int_0^T \boldsymbol{E}' \cdot (\boldsymbol{E} - \boldsymbol{E}^{(\mathrm{m})}) \,\mathrm{d}t \,\mathrm{d}\tau = -\int_0^T \int_\Omega \epsilon' \widetilde{\boldsymbol{E}} \cdot \partial_t \boldsymbol{E} + \mu' \widetilde{\boldsymbol{E}} \cdot \partial_t \boldsymbol{H} + \sigma' \widetilde{\boldsymbol{E}} \cdot \boldsymbol{E} \,\mathrm{dV}\,\mathrm{d}t \quad (6.8)$$

where the definition (6.7) of the adjoint current has been used.

The first order perturbation of the misfit functional is

$$\begin{aligned} \mathcal{J}'[\epsilon,\mu,\sigma] &= -2 \sum_{\text{measurements}} \int_0^T \int_\Omega \epsilon' \widetilde{\boldsymbol{E}} \cdot \partial_t \boldsymbol{E} + \mu' \widetilde{\boldsymbol{H}} \cdot \partial_t \boldsymbol{H} + \sigma' \widetilde{\boldsymbol{E}} \cdot \boldsymbol{E} \,\mathrm{dV}\,\mathrm{d}t \\ &= \langle G_\epsilon, \epsilon' \rangle + \langle G_\mu, \mu' \rangle + \langle G_{\sigma/\langle\sigma\rangle}, \sigma'/\langle\sigma\rangle \rangle \end{aligned} \quad (6.9)$$

where $\langle \cdot, \cdot \rangle$ is the inner product in $\mathrm{L}^2(\Omega)$. In (6.9), a scaling $\langle\sigma\rangle$ of the conductivity is introduced. The scaling is used to average the different components of the gradient [9]. The gradient is identified from (6.9), *i.e.*,

$$\boldsymbol{G}(\boldsymbol{x}) = (G_\epsilon(\boldsymbol{x}), G_{\sigma/\langle\sigma\rangle}(\boldsymbol{x}), G_\mu(\boldsymbol{x}))$$

where

$$\begin{cases} G_\epsilon(\boldsymbol{x}) &= -\sum_{\text{measurements}} 2 \int_0^\Upsilon \int_0^T \widetilde{\boldsymbol{E}}(\boldsymbol{x},t,m) \cdot \partial_t \boldsymbol{E}(\boldsymbol{x},t,m) \,\mathrm{d}t \,\mathrm{d}\tau, \\ G_{\sigma/\langle\sigma\rangle}(\boldsymbol{x}) &= -\sum_{\text{measurements}} 2\langle\sigma\rangle \int_0^\Upsilon \int_0^T \widetilde{\boldsymbol{E}}(\boldsymbol{x},t,m) \cdot \boldsymbol{E}(\boldsymbol{x},t,m) \,\mathrm{d}t \,\mathrm{d}\tau, \\ G_\mu(\boldsymbol{x}) &= -\sum_{\text{measurements}} 2 \int_0^\Upsilon \int_0^T \widetilde{\boldsymbol{H}}(\boldsymbol{x},t,m) \cdot \partial_t \boldsymbol{H}(\boldsymbol{x},t,m) \,\mathrm{d}t \,\mathrm{d}\tau \end{cases} \quad (6.10)$$

The gradient points in the direction towards the fastest growth of the misfit functional. Hence, the parameters are updated in the opposite direction of the gradient. Observe the similarities with SAR imaging, *i.e.*, gradients are given by correlating the illuminating wave field with the back propagated wave field. Hence, the SAR imaging algorithm can be considered as an initial iteration of a least-squares inversion algorithm.

The gradients with respect to general constitutive relations are derived in a similar fashion. For the SAR application, anisotropic material parameters are of particular importance. In the case of an anisotropic non-dispersive permittivity, the first order perturbation of the least-square functional contains the factor

$$\widetilde{\boldsymbol{E}} \cdot \boldsymbol{\epsilon} \partial_t \boldsymbol{E} = \sum_{i=1}^3 \widetilde{E}_i \sum_{j=1}^3 \epsilon_{ij} \partial_t E_j = \sum_{i=1}^3 \sum_{j=1}^3 \widetilde{E}_i \partial_t E_j \epsilon_{ij} \quad (6.11)$$

and hence the gradient

$$G_{ij}(\boldsymbol{x}) = -2 \sum_{\text{measurements}} \int_0^\Upsilon \int_0^T \widetilde{E}_i(\boldsymbol{x},t) \partial_t E_j(\boldsymbol{x},t) \,\mathrm{d}t \,\mathrm{d}\tau \quad (6.12)$$

In the case of a homogeneous background, closed form solutions can be used for the illuminating field and the adjoint field. This gives a gradient similar to back propagation in classical SAR imaging, see *e.g.*, [19]. To simplify the result, a Fourier syntheses is used. The first term in the integral is usually removed by the use of the far-field pattern. Observe, the similarities with the linearized SAR inversion algorithm (4.13). For the SAR application it is natural to consider better initial approximations than a homogeneous region, *e.g.*, a layered model could easily be used.

To iterate the algorithm it is necessary to use a numerical solver to compute the illuminating wave field and the back-propagated (adjoint) wave field. The finite-difference time-domain (FDTD) method is well suited for the computations [16]. In the FDTD calculation, it is advantageous to use a formulation with Huygens' surfaces for the illuminating wave fields and near to far-field transformations for the scattered field.

7 Conclusions

In this paper it is shown that the SAR point scattering model has to be generalized when a large aperture angles are considered. A dipole scattering model is shown to give consistent results for these cases. The dipole model is related to an anisotropic reflectivity.

The preferred setup for a SAR system depends on several factors. In general it is difficult to obtain sufficient data to satisfy the uniqueness criteria in Section 2.2. However, it is likely to have sufficient amount of data such that the simple scalar imaging algorithm is no longer valid. Hence, it it important to have a simple model such that the data can be used consistently. Considering the case of limited data and a linear inversion it is desired to obtain a setup with a large spectral coverage. For the radial coverage it is observed that is it preferable to use a large bandwidth and a high frequency. The angular coverage is given by a large aperture angle. Here it is also observed that the backscattering direction gives the most efficient angular coverage. The forward scattering direction gives limited coverage. For the polarization it is observed that a vertically polarized antenna it preferable to a horizontally polarized antenna. However, it is of course even better to have dual polarized antennas.

Acknowledgments

Lars Ulander and Torleif Martin at the Swedish defence research agency (FIO) are gratefully acknowledged for the valuable discussions about SAR and for the synthetic SAR data.

The financial support by FOI is also gratefully acknowledged.

References

[1] R. Bamler and P. Hartl. Synthetic aperture radar interferometry. *Inverse Problems*, **14**, R1–R54, 1998.

[2] B. Borden. Some issues in inverse synthetic aperture radar imaging. *Inverse Problems*, **13**, 571–584, 1997.

[3] B. Borden. Mathematical problems in radar inverse scattering. *Inverse Problems*, **18**, R1–R28, 2002.

[4] M. Brandfass, A. D. Lantermann, and K. Warnick. A comparison of the Colton-Kirsch inverse scattering method with linearized tomographic inverse scattering. *Inverse Problems*, **17**, 1797–1816, 2001.

[5] F. Collino, M. Fares, and H. Haddar. Numerical and analytical studies of the linear sampling method in electromagnetic inverse scattering. *Inverse Problems*, **19**, 1279–1298, 2003.

[6] D. Colton and R. Kress. *Inverse Acoustic and Electromagnetic Scattering Theory*. Springer-Verlag, Berlin, 1992.

[7] G. Franceschetti and R. Lanari. *Synthetic Aperture Radar Processing*. CRC Press, Boca Raton, 1999.

[8] M. J. Gerry, L. C. Potter, I. J. Gupta, and A. van der Merwe. A parametric model for synthetic aperture radar measurements. *IEEE Trans. Antennas Propagat.*, 1999.

[9] M. Gustafsson. *Wave Splitting in Direct and Inverse Scattering Problems*. PhD thesis, Lund Institute of Technology, Department of Electromagnetic Theory, P.O. Box 118, S-221 00 Lund, Sweden, 2000. `http://www.es.lth.se/home/mats`.

[10] H. Hellsten and L.-E. Andersson. An inverse method for the processing of synthetic aperture radar data. *Inverse Problems*, **3**, 111–124, 1987.

[11] R. Kress. Newton's method for inverse obstacle scattering meets the method of least squares. *Inverse Problems*, **19**, S91–S104, 2003.

[12] G. Kristensson. *Spridningsteori med antenntillämpningar*. Studentlitteratur, Lund, 1999. (In Swedish).

[13] E. Krogager. *Aspects of Polarimetric Radar Imaging*. PhD thesis, Danish Defence Research Establishment, Lyngby, Denmark, 1993.

[14] S. N. Markarov. *Antenna and EM modeling with Matlab*. John Wiley & Sons, New York, 2002.

[15] R. Marklein, K. Balasubramanian, A. Qing, and K. J. Langenberg. Linear and nonlinear iterative scalar inversion of multi-frequency multi-bistatic experimental electromagnetic scattering data. *Inverse Problems*, **17**, 1597–1610, 2001.

[16] T. Martin and L. Ulander. VHF/UHF synthetic aperture radar image simulations of a vehicle using FDTD. Technical Report FOA-R–00-01765-408–SE, FOA Defence Research Establishment, Division of Sensor Technology, P.O. Box 1165, SE-581 11, Linköping, Sweden, 2000.

[17] T. Martin and L. M. H. Ulander. Bistatic SAR pilot study: Simulations using FDTD. Technical Report FOI-R–0839–SE, FOI Swedish Defence Research Agency, Sensor Technology, P.O. Box 1165, SE-581 11, Linköping, Sweden, 2003.

[18] C. J. Nolan and M. Cheney. Synthetic aperture inversion. *Inverse Problems*, **18**, 221–235, 2002.

[19] L. M. H. Ulander, H. Hellsten, and G. Stenström. Synthetic-aperture radar processing using fast factorized back-projection. *IEEE Trans. Aerospace and Electronic Systems*, **39**(3), 760–776, 2003.